ISTANBUL TECHNICAL UNIVERSITY ★ GRADUATE SCHOOL OF SCIENCE ENGINEERING AND TECHNOLOGY

QUALITATIVE METHODS IN MICROWAVE IMAGING

Ph.D. THESIS

Mehmet Nuri AKINCI

Department of Electronics and Communication

Telecommunication Engineering

DECEMBER 2016

ISTANBUL TECHNICAL UNIVERSITY ★ GRADUATE SCHOOL OF SCIENCE ENGINEERING AND TECHNOLOGY

QUALITATIVE METHODS IN MICROWAVE IMAGING

Ph.D. THESIS

Mehmet Nuri AKINCI
(504132302)

Department of Electronics and Communication

Telecommunication Engineering

Thesis Advisor: Associate Prof. Dr. Mehmet ÇAYÖREN

DECEMBER 2016

İSTANBUL TEKNİK ÜNİVERSİTESİ ★ FEN BİLİMLERİ ENSTİTÜSÜ

MİKRODALGA İLE GÖRÜNTÜLEMEDE NİTEL YÖNTEMLER

DOKTORA TEZİ

Mehmet Nuri AKINCI
(504132302)

Elektronik ve Haberleşme Mühendisliği Anabilim Dalı

Telekomunikasyon Programı

Tez Danışmanı: Doç. Dr. Mehmet ÇAYÖREN

ARALIK 2016

Mehmet Nuri AKINCI, a Ph.D. student of ITU Graduate School of Science Engineering and Technology student ID 504132302, successfully defended the thesis/dissertation entitled "QUALITATIVE METHODS IN MICROWAVE IMAGING", which he prepared after fulfilling the requirements specified in the associated legislations, before the jury whose signatures are below.

Thesis Advisor :	**Associate Prof. Dr. Mehmet ÇAYÖREN** İstanbul Technical University	.....
Jury Members :	**Prof. Dr. İbrahim AKDUMAN** İstanbul Technical University	.....
	Prof. Dr. Hülya ŞAHİNTÜRK Yıldız Technical University	.....
	Prof. Dr. Ali YAPAR İstanbul Technical University	.....
	Prof. Dr. M. İrşadi Aksun Koç University	.....

Date of Submission : 18.10.2016
Date of Defense : 05.12.2016

To my parents Haluk and Meryem,

FOREWORD

Gratitude is owed to many individuals who have helped me in one way or another over the past four years, often without knowing they were doing so.

I am very grateful to Associate Prof. Mehmet Çayören and Prof. İbrahim Akduman more for their supportive and thoughtful suggestions during the period of my study. I would like to thank them for giving me the opportunity to work for his project, where I gained great knowledge and experience on microwave imaging.

I extend my gratitude to my father Haluk, mother Meryem, my wife Fatma and my brothers Ekrem and Murat, who gave me tremendous support and deserve much more than a simple thank you. I owe them a lot and will be grateful to them all my life.

I wish to thank several friends who worked closely with me during my study. Dr. Mehmet Abbak, Ph.D., Selçuk Özgür, İsmail Dilman, and Agah Oktay Ertay, M.Sc. many thanks for your wonderful friendship. Special thanks goes to Selçuk Özgür and Dr. Mehmet Abbak for their friendship and wonderful support.

December 2016

Mehmet Nuri AKINCI
Electronics and Communication
Engineer, B.Sc.

TABLE OF CONTENTS

Page

ABBREVIATIONS

MWI : Microwave Imaging
LSM : Linear Sampling Method
FM : Factorization Method
CSI : Contrast Source Inversion
DBIM : Distorted Born Iterative Method
FFT : Fast Fourier Transform
BiCG-FFT : Biconjugate Gradient Fast Fourier Transform
GPR : Ground Penetrating Radar
VNA : Vector Network Analyzer
ITU-ERG : Istanbul Technical University Electromagnetic Research Group

SYMBOLS

$\mathbf{E}$	**:** Electric Field (V/m)
$\mathbf{B}$	**:** Magnetic Induction (T)
$\mathbf{D}$	**:** Displacement Vector (C/m^2)
$\mathbf{H}$	**:** Magnetic Field (A/m)
$\boldsymbol{\rho}$	**:** Charge Density (C/m^3)
$\mathbf{J}$	**:** Current Density (A/m^2)
$\boldsymbol{\epsilon_0}$	**:** Dielectric Permittivity of the Vacuum (F/m)
$\boldsymbol{\mu_0}$	**:** Magnetic Permeability of the Vacuum (Tm/A)
$\boldsymbol{\epsilon_r}$	**:** Relative Permittivity of a Medium (-)
$\boldsymbol{\mu_r}$	**:** Relative Permeability of a Medium (-)
$\boldsymbol{L^2(\Omega)}$	**:** Hilbert Space Defined on the Surface $\boldsymbol{\Omega}$
$\|\| \cdot \|\|_{\boldsymbol{L^2(\Omega)}}$	**:** Euclidean Norm in $\boldsymbol{L^2(\Omega)}$

LIST OF TABLES

Page

LIST OF FIGURES

Page

QUALITATIVE METHODS IN MICROWAVE IMAGING

SUMMARY

Microwave imaging (MWI) emerges as a novel technology that aims to extract physical properties of inaccessible objects from the scattered electric field measurements. MWI covers a very wide range of applications which includes but not limited to nondestructive testing (NDT), subsurface imaging, through wall imaging, biological imaging. The most important factor that tends the scientists to imaging with microwaves is non-ionizing nature of MWI when interacted with biological tissues. Therefore, MWI can be regarded as a healthy alternative of current imaging technologies, which are mostly based on ionizing radiation.

Inverse scattering theory provides a group of highly theoretical approaches, known as qualitative method. These methods are based on inverting an integral equation for each point over a reconstruction domain to determine only the shape and the position of unknown scatterers without requiring any a-priori information. Two well-known representatives of qualitative inverse scattering methods are (i) linear sampling method (LSM) and (ii) factorization method (FM). These two methods are in fact quite similar in formulation as well as performance. These qualitative approaches are also usable in the MWI, where the inverse problem can be casted into two integral equations.

Traditional solution approaches for MWI are based on non-linear or linear optimization methods. These methods recasts the nonlinear scattering problem in form of a minimization problem. Additionally, they can utilize Born approximation to linearize the problem and then the cost function is minimized via one of the canonical optimization approaches such as conjugate gradient method, newton's method. In other words, these methods model the physical scattering mechanism to determine electrical properties of dielectric objects and attempts to minimize a cost functional by using a canonical minimization procedure. In contrast to these approaches, the qualitative inverse scattering methods uses linearity of the scattering problem or the duality principle to reach their final aim, which is obtaining the support of the scatterer. Thus, their modest goals and linear nature make these qualitative approaches easier to implement and more efficient in use of computational resources. In contrast to all these attractive features, both LSM and FM are rarely investigated from an engineering perspective due to their mathematical background. Hence, analyzing these methods from an engineering perspective and making these methods applicable in real world imaging scenarios is an important problem.

In the first part of the thesis, we analyze the problem of imaging buried targets under a rough surface for a two dimensional transverse magnetic scattering scenario. In fact, imaging of buried targets under the rough ground is a challenging inverse scattering problem with many applications in engineering such as land mine detection and remote sensing of archaeological artefacts. Conventional technology that uses microwaves for subsurface sensing of the underground is ground penetrating radar (GPR) which generates radargrams that require further interpretation by experts. Also, various quantitative inverse scattering methods are existent in the literature to provide

additional information on the morphological and electrical properties of buried obstacles. Furthermore, the surface roughness, which is a critical factor that determines the limits of subsurface imaging, are only considered in a very few studies. In this context, qualitative inverse scattering methods, which are almost exclusively used for reconstructing the shape of inaccessible targets from the scattered field measurements, are particularly interesting since such methods can image multiple objects without requiring a-priori knowledge. Thus, we present a qualitative imaging method for subsurface sensing under a rough surface. The method relies on FM, where the aim is to retrieve the shape of unknown dielectric objects embedded inside a dielectric body whose closed boundary and electrical parameters are known a priori. Results show the stability and accuracy of the proposed method under very realistic conditions.

In the second part of this thesis, the problem of using the qualitative methods in the real world measurement scenario is addressed. In the real world applications imaging systems extensively incorporate vector network analyzers (VNAs) instead of implementing additional modules to perform microwave measurements. This is particularly driven by availability of high performance VNAs. While there are alternative ways of reconstructing an image in MWI, imaging methods are naturally formulated in terms of scattered electric field vectors whereas measured scattering parameters (S-parameters) are only auxiliary quantities. Consequently, an intermediate step is required for experimental setups where measured S-parameters are mapped into scattered electric field. This is mostly handled by comparing simulated electric fields against measured S-parameters. As a better alternative to the canonical calibration procedures, we develop novel qualitative microwave imaging algorithms, which uses the measured S-parameters directly. Obtained experimental results prove the accuracy and the stability of the presented method.

In the third and last part of the thesis, we consider the problem of using qualitative imaging methods in real world concealed target imaging scenarios. Real world concealed target detection can have different applications ranging from medical imaging to subsurface sensing, as mentioned above. Main challenge for such inverse problems is that the solution procedures are expected to capture the electrical parameters (relative dielectric constant ϵ_r, conductivity σ) of whole medium, which includes the buried objects. Up to date, many quantitative techniques are developed to obtain the complete electrical parameter distribution of a medium. However, if we take a glance at these formulations, we can see that they involve a considerable computational burden. Being contradictory to quantitative techniques, qualitative inversion methods, which aim to recover only the shape of the scatterers, have relatively simple formulations and require lower computational resources. In contrast to such obvious advantages, qualitative inversion techniques are rarely employed in buried obstacle detection, since these methods have strong a priori knowledge requirements in their original form. In particular, to be able to detect the shape of an inclusion by means of these methods, we must supply these two a priori pieces of information: (i) the dielectric parameters of the surrounding medium and (ii) the scattered field when there is no buried object inside the surrounding medium. It is obvious that fulfilling such strong conditions altogether is of a serious issue in any imaging problem. To this end, we propose a strategy to overcome the a priori knowledge requirement on the dielectric parameters of the surrounding medium. Results, which are obtained from real experiments performed in an anechoic chamber, confirm the accuracy and the stability of the proposed formulations.

MİKRODALGA GÖRÜNTÜLEMEDE NİTEL YÖNTEMLER

ÖZET

Mikrodalga görüntüleme doğrudan erişilemeyen saçıcıların elektriksel özelliklerini (göreli dielektrik sabiti ϵ_r, göreli manyetrik geçirgenlik katsayısı μ_r iletkenlik σ yahut debye parametreleri) saçtıkları elektrik alandan tespiti ile ilgilenen yeni bir teknolojidir. Mikrodalga görüntüleme hasarsız muayene, toprak altı görüntüleme, duvar arkası görüntüleme ve biyolojik doku görüntüleme gibi çeşitli tıbbi ve askeri uygulamalarda gelecek vaadeden bir teknikdir. Mikrodalga görüntülenmenin günümüz biliminde bu denli önemli olmasının temel nedeni ise biyolojik dokularla etkileşime geçtiğinde ionize edici bir özelliği olmamasıdır. Bu nedenle mikrodalga görüntüleme günümüzde sıkça kullanılan ve çoğu ionize edici radrasyona bağlı olan görüntüleme teknolojilerinin tümü için çok önemli bir yedek seçenektir.

Ters saçılma teorisi nitel görüntüleme yöntemleri adı altında oldukça teorik bir takım yöntemleri literatürde barındırmakradır. Nitel görüntüleme yöntemleri integral denklemlerden saçıcının yalnızca şekil ve konumunun tespiti için kullanılır olup ve saçıcıların yapısı ve şekli ile ilgili herhangi bir ön bilgiye ihtiyaç duymamaktadır. Nitel görüntüleme yöntemlerinin en bilindik iki tanesi: (i) doğrusal örnekleme yöntemi ve (ii) faktörizasyon yöntemidir. Doğrusal örnekleme yöntemi ve faktörizasyon yöntemi formülasyon ve performans açısından birbirine oldukça benzerdir. Kısaca anlatmak gerekirse, doğrusal örnekleme yöntemi tarihsel olarak faktörizasyon yönteminden önce önerilmiş olup henüz matematiksel olarak tam olarak ispat edilememiştir. Faktörizasyon yöntemi ise doğrusal örnkeleme yönteminden esinlenerek geliştirilmiş olup doğruluğu matematiksel olarak da kanıtlanmıştır. Bu iki yönteminde ters problemin birbirine bağlı iki doğrusal olmayan integral denklem olarak ifade edilebildiği mikrodalga görüntülemede kullanılması mümkündür.

Mikrodalga görüntülemede geleneksel çözüm yolu doğrusal olan veya doğrusal olmayan optimizasyon metodlarıdır. Bu metotlar eldeki doğrusal olmayan elektromanyeik saçılma problemini bir minimizasyon problemi haline dönüştürür. Ek olarak bu yöntemlerin bazıları doğrusal olmayan saçılma problemini doğrusal hale getirebilmek amacıyla Born yaklaşımını da kullanır. Sonuç olarak eldeki amaç fonksiyonunu minimize etmek amacıyla bilindik bir optimizasyon yöntemini (konjuge gradyan metodu, Newton yöntemi vs.) kullanır. Diğer bir deyişle nicel görüntüleme yöntemi olan bu metotlar fiziksel saçılma mekanizmasını kullaranarak elde edilen ölçülmüş elektrik alanı oluşturacak saçıcının şeklini ve elektriksel özelliklerini (göreli dielektrik sabiti ϵ_r, göreli manyetrik geçirgenlik katsayısı μ_r iletkenlik σ yahut debye parametreleri) kestirmeye çalışır. Bu nicel yöntemlerin dışında bir de yukarıda da bahsettiğimiz nitel görüntüleme yöntemleri vardır ki bunlar saçılma problemini sadece saçıcıların şeklini ve konumunu bulmak amacıyla çözerler. Nitel görüntülenme yöntemleri, nicel görüntüleme metotlarından farklı olarak hedef cisimlerin şekli ve konumunu tespit amacıyla genellikle elektromanyetik saçılma probleminin belirli bir saçıcı veya saçıcılar kümesi için doğrusal olması gerçeğini ve dualite prensiplerini

kullanır. Nitel görüntüleme yöntemlerinin bu görece düşük beklentisi ve doğrusal yapıları onların bilgisayar ortamında kolayca gerçeklenebilmesini ve nicel görüntüleme yöntemlerine oranla çok daha az sürelerde ve çok daha az bir hesaplama yükü ile bilgisayar ortamında çalıştırılabilmesini sağlar. Tecrübelerimize dayanarak örnek vermek gerekirse, üç boyutlu (yaklaşık 150 bin – 300 bin bilinmeyen içeren) bir saçılma probleminin kontrast kaynak yöntemi ile çözülmesi ortalama bir bilgisayarda (8 GB RAM) olarak 1-2 saat alırken, aynı probleme LSM veya FM'nin uygulanması için maksimum 5 – 10 dk. gibi bir süre yeterli olacaktır. Tüm bu avantajalrına rağmen, başta LSM ve FM olmak üzere tüm nitel görüntüleme yöntemleri mühendislik alanında çok da uygulama alanı bulamamaktadır. Bunun başlıca sebepleri nitel görüntüleme yöntemlerinin genellikle çok üst düzey bir matematiksel arkaplana dayanması, bu yöntemlerin matematikçiler tarafından fiziksel şartların ve gerçek hayat durumlarının pek de düşünülmeden ortaya konulmuş olması (yani bu yöntemlerin pek çoğu esas olarak düzlem dalga aydınlatması altında ve ölçümlerin ölçüm mesafesi sonsuza yaklaşırkenki asimptotik halleri için kanıtlanmıştır) ve bu yöntemlerin fiziksel bir zemine oturtulmasının zor olmasıdır. İşte bu sebeblerle nitel görüntüleme yöntemlerinin incelemesi ve nitel görüntüleme yöntemlerinin gerçek hayatta kullanabileceğimiz algoritmalar haline getirilip onların fiziksel arkaplanlarının ve uygulama için gerekli koşulların ortaya konulması önemli bir çalışma alanı teşkil etmektedir.

Bu tezin ilk kısmında, iki boyutlu bir uzayda enine manyetik saçılma senaryosu için engebeli bir yüzey altındaki gömülü cisimlerin tespiti amacıyla bir faktörizasyon metodu önerilmiş ve benzetimlerle elde edilmiş sonuçlarla oldukça gerçekçi durumlar için doğrulanmıştır. Esasında engebeli yüzey altında gömülü cisimlerin görüntülenmesi mayın tespiti ve arkelojik gömülerin görüntülenmesi gibi çok değişik uygulamaları olan oldukça karmaşık bir problemdir. Günümüzde yeraltının görüntülenmesi için mikrodalgaları kullanan temel teknoloji uzmanlar tarafından yorumlanması gereken ve sonuçta radaragramlar oluşturan yer radarı (ground penetrating radar, GPR) olduğu bilinmektedir. Bunun haricinde görüntülenmek istenen yeraltı bölgenin elektriksel ve şekilsel özellikleri ile ilgili bilgi veren bazı nitel ters saçılma yöntemleri de literatürde bulunmaktadır. Ayrıca, yeraltı görüntülemede çok önemli bir faktör olan ve çoğu zaman uygulanan yöntemin başarısını belirleyen yüzey engebesinin ise pek az sayıda çalışmada dikkate alındığı gerçeği de bilinmektedir. Bu bağlamda, pek çok görüntüleme probleminde saçıcı cisimlerin yer ve şeklinin tespiti amaçlı kullanılabilecek olan ve aynı anda pek çok sayıda değişik özelliğe sahip saçıcıları da görüntüleyebilen nicel mikrodalga görüntüleme yöntemleri bu problem özelinde de (engebeli bir yüzey altında gömülü saçıcı hedeflerin tespiti) oldukça ilginç bir alternatif teşkil etmektedir. Bundan dolayı tezimizin ilk kısmı bu konu üzerine olan çalışmalarımıza ayrılmıştır. Özel olarak bu kısımda yeraltına gömülü herhangi bir sayıda ve herhangi bir özelliğe sahip saçıcıların yer ve konumları faktörizasyon metodu ile tespit edilecektir. Çalışmamızda sınırlı açıklıklı bir anten dizisi ile belirli bir toprak altı bölgenin taranması durumu değişik aydınlatma frekansları, değişik nem oranına haiz toprak, değişik engebe profilleri, toprağın ve engebe profillerinin kısmen bilindiği durumlar için ayrı ayrı incelenmiş olup her durumda yöntemin başarımı ortaya konmuştur. Elde edilen sonuçlar uygulanan yöntemin gerçek hayattaki problemler için de umut verici olduğunu ortaya koymuştur.

Tezin ikinci kısmında ele alınan temel nicel görüntüleme yöntemlerinin gerçek ölçüm düzenekleri için nasıl kullanılacağı problemi ele alınmıştır. Mikrodalga frekanslarında yapılan ölçümlerde yaygın olarak vektör ağ analizörleri (vector network analyzer,

VNA) kullanımaktadır. Bu yaygın kullanımın başlıca sebebi vektör ağ analizörlerinin piyasada kolayca bulunabilir oluşu ve bu cihazların gösterdiği yüksek performansdır. Birkaç istisnai durum haricinde mikrodalga görüntüleme problemleri hep saçılan elektrik alan bilgisini kullanıp saçıcı hedeflerin elektriksel parametrelerinin (göreli dielektrik sabiti ϵ_r, göreli manyetrik geçirgenlik katsayısı μ_r iletkenlik σ yahut debye parametreleri) hesaplanmasını amaçlar. Buna karşın, vektör ağ çözümleyicilerinin ölçtüğü temel büyüklük saçılma parametreleridir. Bu nedenle genellikle yapılan iş ölçülen saçılma parametrelerinin saçılan elektrik alana çevrilmesi için belli başlı prosedürleri uygulamaktır. Saçılma parametreleri ile saçılan elektrik alan arasındaki bu bağlantıyı sağlayan dönüşüm ise genellikle belirli bir geometrik şekle haiz (düzlem, düzgün dairesel silindir veya küre) ve bilindik elektriksel özellikteki cisimlerin ölçülen saçılma parametreleri ile benzetimden elde edilmiş saçılan elektrik alanını karşılaştırmak üzerine kuruludur. Tezin ikinci kısmında bu bilindik kalibrasyon prosedürlerinin yerine daha iyi bir alternatif olarak ele alınan nitel görüntüleme yöntemlerini (doğrusal örneklem yöntemi ve faktörizasyon yöntemi) doğrudan saçılma parametreleri üzerinden yendien formüle ettik. Elde edilen sonuçlar geliştirlen yöntemin hem iki boyutlu hem de üç boyutlu görüntüleme de çok satbil ve doğru bir şekilde çalıştığını göstermektedir.

Tezin üçüncü ve son kısmında ise ele alınan nitel görüntüleme yöntemleri (doğrusal örneklem yöntemi ve faktörizasyon yöntemi) ile saklı cisim tespiti probleminin çözümü üzerine yoğunlaştık. Saklı cisim tespiti problemi gerçek hayat uygulamalarında, özellikle çeşitli medikal ve askeri uygulamalarda, pek çok durumda karşımıza çıkmaktadır. Saklı cisim tespiti problemleminin çözümündeki temel zorluk ele alınan (görüntülenmesi hedeflenen) ortamın her noktasındaki elektriksel parametrelerin (göreli dielektrik sabiti ϵ_r, göreli manyetrik geçirgenlik katsayısı μ_r iletkenlik σ yahut debye parametreleri) hesaplanmasının gerekliliğidir. Bugüne kadar ele alınan ortamın tüm elektriksel parametrelerinin her noktadaki hesabı için pek çok değişik nicel görüntülüme yöntemi geliştirilmiş ve doğrulanmıştır. Ancak tüm nicel görüntüleme yöntemleri gibi bu yöntemlerinde oldukça ağır bir hesaplama yükü içerdiği gerçeği ortadadır. Daha önce de bahsedildiği üzere nicel yöntemlerin aksine nitel görüntüleme yöntemleri daha basit şekilde bilgisayar ortamında gerçeklenebilen daha basit formülasyonlara sahip ve hesaplama zamanı ve yükü nicel görüntüleme yöntemlerine oranla oldukça düşük olan yöntemlerdir. Tüm bu avantajlarına rağmen nitel görüntüleme yöntemleri saklı cisim tespitinde oldukça az kullanılmıştır. Bunun başlıca sebepleri, yukarıda da bahsedildiği üzere, bu yöntemlerin çok üst düzey bir matematiksel arkaplana dayanması, nitel görüntüleme yöntemlerinin matematikçiler tarafından fiziksel şartların ve gerçek hayat durumlarının pek de düşünülmeden ortaya konulmuş olması ve bu yöntemlerin fiziksel bir zemine oturtulmasının zor olmasıdır. Özel olarak saklı cisim tespiti problemi için bakacak olursak, nitel görüntüleme yöntemleri saklı cisim tespiti probleminde şu iki temel bilgiye ihtiyaç duyar: (i) cisimlerin gömülü olduğu ortamın elektriksel özellikleri (göreli dielektrik sabiti ϵ_r, göreli manyetrik geçirgenlik katsayısı μ_r iletkenlik σ yahut debye parametreleri) (ii) gömülü cisimlerin olmadığı duumda arka plandan saçılan elektrik alan bilgisi. Açıktır ki bu iki bilginin her ikisini de aynı anda sağlamak neredeyse tüm problemler için imkansızdır. Bu sebeple biz tzin bu üçüncü ve son kısmında bu önsel bilgi probleminin çözümü amacıyla bir yöntem önerdik. Özel olarak, pek çok saklı cisim tespiti probleminde yukarıdaki ikinci bilgi ((ii) gömülü cisimlerin olmadığı duumda arka plandan saçılan elektrik alan bilgisi) aslında elde edilebilir olup bu bilgi ışığında ilk önsel bilgiyi kullanmadan eldeki nitel görüntüleme yöntemlerinin yüksek bir

başarımla çalıştırılabileğini önerdik. Elde edilen sonuçlar önerdiğimiz yöntemin oldukça stabil ve doğru bir biçimde çalıştığını doğrular niteliktedir.

1. INTRODUCTION

Microwave imaging is an important and newly developing technology for specialized needs arising in military, medical and other applications. Microwaves have important advantages when compared with other conventional imaging modalities. Firstly, many imaging technology, which are consistently employed in military and medical area, highly depends on ionizing radiation, which is quite harmful for health. Microwaves do not have an ionizing property, thus regardless of the the final aim, the developed method will not as harmful as the currently used modalities. Furthermore, the wavelengths utilized in microwaves are well suitable (i.e. are resonance with targets) for many real world applications while they can penetrate into biological tissues (for medical applications), in soil (for subsurface imaging) and in air (for radar and military applications). In contrast to such advantages, using microwaves raises several problems, which constitutes the basis of many researches made on microwave imaging technologies today. The first and biggest problem is that the imaging with microwaves requires solving Maxwell's equation for scatterers having sizes in the order of wavelength (i.e. in resonance region). Unfortunately, the electromagnetic scattering problem is turned out to be a nonlinear problem in resonance region, while imaging with higher frequencies, which are mostly used in the many imaging modalities like computerized tomography, can generally be modeled with linear scattering problem approximations. Thus, microwave imaging requires specialized algorithms, which can handle with nonlinear optimization problems. It is obvious that these improved algorithms will take certainly more time to be solved and will occupy more computational space in any computer system. Additionally, the systems that are to be designed for microwave imaging operations can have relatively large sizes and their calibration requires additional operations. Nevertheless, in the recent years many researches prove that with the increasing computational power of the commercially available computers, it will be possible to solve these problems in a near future.

Microwave imaging technologies can mainly be separated into two different groups: (i) quantitative inversion methods [1-7] (ii) qualitative inversion methods [8-14]. First group of methods aim to recover the electrical parameters (relative dielectric constant ϵ_r, relative magnetic permeability μ_r, conductivity σ or debye parameters) of the investigated region. By doing so, such methods can retrieve all information (shape, location and electrical parameter distribution) of the whole investigated region. Quantitative inversion approaches either set the non-linear scattering problem as minimization of a non-linear function [2-5] or they utilize from Born approximation [1,2] and/or the concept of virtual experiments [6,7] to convert the scattering problem into minimization of a linear function. After setting up the optimization problem, quantitative inversion methods employ canonical minimization-maximization procedures like conjugate gradient method, Newton's method to obtain the most suitable electrical parameter distribution, which can generate the measured scattered electric field under given incident field excitation. Examples of these methods includes but not limited to Contrast Source Inversion method [3-5], Born Iterative method [1,2], Distorted Born Iterative method [2]. Quantitative imaging methods are shown to be stable and accurate for many practical microwave imaging problems [1-7]. In contrast to such advantageous the quantitative inversion methods, they generally require a significant amount of computational time-computational space and due to these large computational requirements their implementation are not generally straightforward in any computer system. Specifically, there are ongoing researches on how to implement the quantitative inversion methods more efficiently [6,7,15-18]. Possible solutions include but not limited to using parallel computing approaches [15,16], reducing computational size of the scattering problem via certain assumptions like virtual experiments technique [6,7], sparsity constrained optimization techniques [17,18].

Qualitative inversion approaches aim to retrieve only the shape and the location of the scatterers and they do not provide information about the electrical properties (relative dielectric constant ϵ_r, relative magnetic permeability μ_r, conductivity σ or debye parameters) of the targets [8-14]. For this aim, qualitative inversion methods utilize from the fact that the scattering problem is linear when the scatterer remains the same and they also employ duality/reciprocity principles to obtain so called indicator functions, which have the information of the shape and the location of the targets. Examples of qualitative inversion techniques include but not limited to linear sampling

method [9], factorization method [10], point source method [13], no-response test [13]. From those examples, the most remarkable ones are the linear sampling method [9,12,14] and the factorization method [10,11]. The qualitative inverse scattering methods are well established in mathematical literature, but their applications in real world engineering problems are rarely investigated [6,7,14]. The reasons behind this fact are: (i) their sophisticated mathematical background, which highly depends on special subjects of functional analysis (ii) their unrealistic assumptions, which are hard to satisfy in real world applications, e.g. most of those methods are proposed for plane wave excitation and far field measurements, they can require some a-priori information about the target, especially for the concealed target detection problems [13]. Nevertheless, the qualitative inverse scattering methods constitute an important option for microwave imaging problems, when one considers their modest computational time-computational space requirements [13]. Thus investigation of the usability of qualitative inverse scattering methods in real world microwave imaging problems is an important problem, which can find many applications in different areas ranging from medical imaging to military purposes.

1.1 Purpose of Thesis

In the context described above, the general aim of this thesis is to analyze the qualitative imaging methods from an engineering perspective as well as explaining how to use these qualitative approaches in real world imaging problems.

In the first part of the thesis, we analyze the problem of imaging buried targets under a rough surface for a two dimensional transverse magnetic (2D-TM) scattering scenario. In fact, imaging of buried targets under the rough ground is a challenging inverse scattering problem with many applications in engineering such as land mine detection and remote sensing of archaeological artefacts. Conventional technology that uses microwaves for subsurface sensing of the underground is ground penetrating radar (GPR) which generates radargrams that require further interpretation by experts [19]. On the other hand, as we declared above, various quantitative inverse scattering methods have been attempted to generate more intuitive subsurface images of underground as well as providing additional information on the morphological and electrical properties of buried obstacles [19-24]. While the surface roughness is a critical factor that determines the limits of subsurface imaging, very few studies take

surface roughness into account [25,26]. In this context, qualitative inverse scattering methods, which are almost exclusively used for reconstructing the shape of inaccessible targets from the scattered field measurements, are particularly interesting since such methods can image multiple objects without requiring a-priori knowledge [13]. Thus, we present a qualitative imaging method for subsurface sensing. The method relies on the theoretical framework derived in [27], where the aim is to retrieve the shape of unknown dielectric objects embedded inside a dielectric body whose closed boundary and electrical parameters are known a priori.

In the second part of this thesis, the problem of using the qualitative methods in the real world measurement scenario is addressed. In the real world applications imaging systems extensively incorporate vector network analyzers (VNAs) instead of implementing additional modules to perform microwave measurements. This is particularly driven by availability of high performance VNAs. While there are alternative ways of reconstructing an image in MWI, imaging methods are naturally formulated in terms of scattered electric field vectors whereas measured scattering parameters (S-parameters) are only auxiliary quantities. Consequently, an intermediate step is required for experimental setups where measured S-parameters are mapped into scattered electric field. This is mostly handled by comparing simulated electric fields against measured S-parameters [28,29]. As a better alternative to the canonical calibration procedures, we develop novel qualitative microwave imaging algorithms, which uses the measured S-parameters directly.

In the third and last part of the thesis, we consider the problem of using qualitative imaging methods in real world concealed target imaging scenarios. Real world concealed target detection can have different applications ranging from medical imaging to subsurface sensing, as mentioned above. Main challenge for such inverse problems is that the solution procedures are expected to capture the electrical parameters (relative dielectric constant $\boldsymbol{\epsilon_r}$, conductivity σ) of whole medium, which includes the buried objects. Up to date, many quantitative techniques are developed to obtain the complete electrical parameter distribution of a medium [1-7]. However, if we take a glance at these formulations, we can see that they involve a considerable computational burden. Being contradictory to quantitative techniques, qualitative inversion methods, which aim to recover only the shape of the scatterers, have relatively simple formulations and require lower computational resources [8,13]. In

contrast to such obvious advantages, qualitative inversion techniques are rarely employed in buried obstacle detection, since these methods have strong a priori knowledge requirements in their original form. In particular, to be able to detect the shape of an inclusion by means of these methods, we must supply these two a priori pieces of information: (i) the dielectric parameters of the surrounding medium and (ii) the scattered field when there is no buried object inside the surrounding medium [8,13]. It is obvious that fulfilling such strong conditions altogether is of a serious issue in any imaging problem. To this end, we propose a strategy to overcome the a priori knowledge requirement on the dielectric parameters of the surrounding medium.

1.2 Literature Review

For the first part of the thesis, the situation is as we explained in the above. Today's conventional technology utilizes from GPR to obtain a map of the targets buried under soil [19]. In addition to this, there are some works to extent usage of microwaves to localization of buried targets' case [20-24]. Yet, only a small portion of these works consider the case when the surface profile has a roughness, which is the case for many circumstances [25,26]. Thus, in the author's opinion, the contribution of the first part of this thesis, which is applied a recently proposed factorization method for a realistic near field measurement scenario, becomes meaningful.

For the second part of the thesis, the previous works states nothing but using LSM, which is described in [9], or FM, which is introduced in [10,11], after a conventional calibration procedure [1-7]. Yet, this calibration procedure does not take the antenna patterns into account explicitly [1-7]. Also to be able to obtain an image, the S-parameter data must undergo some processing to be converted into electrical field values [1-7]. Thus, in the author's opinion, the contribution of the second part of this thesis, which is developing the S-parameter based linear sampling method (S-LSM) and S-parameter based factorization method (S-FM), becomes meaningful.

Lastly, for the final part, it has to be said that there are already several studies to remedy the a priori information problems of qualitative imaging methods [31-34]. In [31], the reciprocity gap-linear sampling method (RG-LSM) is utilized to relieve LSM from the above mentioned constraints. In [32-34], different qualitative methods are assessed in biomedical applications for which a limited a priori information is available. Yet, the methods, which are presented in the thesis, distinguish from these works. Simply, the

introduced methods proposes a practical solution procedure and they are experimentally verified by means of the real measurements. We stated before that to be able to detect the shape of an inclusion by means of these methods, we must supply these two a priori pieces of information: (i) the dielectric parameters of the surrounding medium and (ii) the scattered field when there is no buried object inside the surrounding medium. Explicitly, we state that it is possible to use LSM and FM in practical situations, whenever the condition (ii) is satisfied. It is important to notice that if (i) is satisfied (ii) is already fulfilled, but the converse is not true. Furthermore, the second condition can be satisfied in certain practical applications like mine sweeping, subsurface sensing or through-wall imaging, and so forth. Thus, in the author's opinion, the contribution of the final part of this thesis, which is giving a practical recipe for application of LSM and FM in real world concealed target imaging scenarios, becomes meaningful.

1.3 Hypothesis

The hypotheses and contributions, which are newly proposed and confirmed in this thesis, can be given as in the below:

1. In the first part of the thesis, we have applied a recently proposed factorization method, which uses far field measurement data inherently, to a rough-subsurface imaging problem, where the measurements are near field.
2. In the first part of the thesis, we have described how this factorization method can be utilized when the exciting-measuring antennas do not cover whole surface (i.e. for the limited aperture situation).
3. In the first part of the thesis, we also analyze the performance of the method for other realistic cases, where the dielectric parameters of the soil or the roughness profile is not exactly known.
4. In the second part of the thesis, we develop the S-parameter based linear sampling method (S-LSM) and S-parameter based factorization method (S-FM), which uses S - parameters measurements instead of electric field measurements.

5. In the second part of the thesis, we define two novel quantity, which are vector S-parameters and dyadic Green's function for S-parameters to develop the S-LSM and S-FM.
6. In the second part of the thesis, we experimentally prove the developed formulations for 2D-TM scattering setup.
7. In the second part of the thesis, we experimentally prove the developed formulations for 3D vectorial scattering setup.
8. In the third part of the thesis, we improve the LSM and FM to cope with real world concealed target imaging problems. In particular we release the methods from their a-priori information requirements.
9. In the third part of the thesis, we experimentally prove the developed formulations for 2D-TM scattering setup

2. MICROWAVE IMAGING

2.1 Direct Scattering Problem

Consider a 3D scattering problem scenario in which several objects $\Omega_1, \Omega_2, \dots, \Omega_P$, which are encapsulated by a domain D and which have with different electromagnetic parameters $(\epsilon_{r1}, \mu_{r1}, \sigma_1), (\epsilon_{r2}, \mu_{r2}, \sigma_2), \dots, (\epsilon_{rP}, \mu_{rP}, \sigma_P)$, are hosted in a background medium, whose electromagnetic parameters are $(\epsilon_{rb}, \mu_{rb}, \sigma_b)$. Assume that this system is excited by the plane wave $\mathbf{E^i}(\mathbf{r}) = \exp(i\mathbf{k_b}.\mathbf{r})$, where $\mathbf{k_b} = k_b\mathbf{n^i}$; $k_b^2 = \omega^2\mu_{rb}\varepsilon_{rb}\mu_0\epsilon_0 + i\sigma_b\mu_{rb}\mu_0\omega$; ω is the angular frequency of illumination and $\mathbf{n^i}$ is the direction of the propagation of the plane wave. Then, Helmholtz equations that has to be satisfied can be given as in the below:

$$\Delta\mathbf{E}(\mathbf{r}) + k^2\mathbf{E}(\mathbf{r}) = 0 \tag{2.1}$$

$$\Delta\mathbf{E^i}(\mathbf{r}) + k_b^2\mathbf{E^i}(\mathbf{r}) = 0 \tag{2.2}$$

where k^2 is wavenumber in the medium containing the scatterers, $\mathbf{E}(\mathbf{r})$ and $\mathbf{E^s}(\mathbf{r}) = \mathbf{E}(\mathbf{r}) - \mathbf{E^i}(\mathbf{r})$ are the total and scattered electrical fields excited in the whole medium.

The below modifications can be done on (2.1) and (2.2):

$$\Delta\mathbf{E}(\mathbf{r}) + k^2\mathbf{E}(\mathbf{r}) = \Delta\mathbf{E^i}(\mathbf{r}) + k_b^2\mathbf{E^i}(\mathbf{r}) + (k^2 - k_b^2)\mathbf{E^i}(\mathbf{r}) + \Delta\mathbf{E^s}(\mathbf{r}) + k^2\mathbf{E^s}(\mathbf{r}) \tag{2.3}$$

$$= (k^2 - k_b^2)\mathbf{E^i}(\mathbf{r}) + \Delta\mathbf{E^s}(\mathbf{r}) + k^2\mathbf{E^s}(\mathbf{r}) = 0 \tag{2.4}$$

Then, the Helmholtz equation for scattered field can be written as:

$$\Delta\mathbf{E^s}(\mathbf{r}) + k_b^2\mathbf{E^s}(\mathbf{r}) = -(k^2 - k_b^2)(\mathbf{E^i}(\mathbf{r}) + \mathbf{E^s}(\mathbf{r})) \tag{2.5}$$

$$(\Delta + k_b^2)\mathbf{E^s}(\mathbf{r}) = -(k^2 - k_b^2)\mathbf{E}(\mathbf{r}) \tag{2.6}$$

Now, solution of the above equation can be simply written as a convolution of the sources (which is the the term at the right hand side) with the Green's function of the Helmholtz equation in the scatterer free space, which is given by:

$$\mathbf{G}(\mathbf{r}, \mathbf{r}') = \left(\mathbf{I} + \frac{1}{k_b^2}\ \boldsymbol{\nabla\nabla}\right)\frac{\exp(ik|\mathbf{r}-\mathbf{r}'|)}{4\pi|\mathbf{r}-\mathbf{r}'|} \tag{2.7}$$

Thus:

$$\mathbf{E^s}(\mathbf{r}) = \int_D (k^2 - k_b^2)\mathbf{G}(\mathbf{r},\mathbf{r}')\,\boldsymbol{\chi}(\mathbf{r}')\mathbf{E}(\mathbf{r}')\boldsymbol{dr}', \quad \mathbf{r} \in \mathbb{R}^3 \tag{2.8}$$

Then by writing the above equation for $\mathbf{r} \in$ D, we can obtain the below Fredholm equation of second kind

$$\mathbf{E}(\mathbf{r}) = \mathbf{E^i}(\mathbf{r}) + \int_D (k^2 - k_b^2)\mathbf{G}(\mathbf{r},\mathbf{r}')\,\boldsymbol{\chi}(\mathbf{r}')\mathbf{E}(\mathbf{r}')\boldsymbol{dr}', \quad \mathbf{r} \in \mathrm{D} \tag{2.9}$$

The above equation is shown to be a well posed problem and its solution can be made by using the traditional method of moments technique [35]. After solving (2.9) and obtaining the total electric field inside the D, we can use (2.8) to compute the scattered field in $\mathbb{R}^3$.

2.2 Computational Aspects of Direct Scattering Problem

Let us select D as the minimal cube containing all P scatterers and say the edge length of the sampling domain D is L. Then, by dividing this sampling domain to N in each orthogonal direction, Q=N^3 many cubic cell is obtained with each of edge length $\frac{L}{N}$. The centers of these cubic cells are selected as our sampling points $\mathbf{r_1}, \mathbf{r_2}, \ldots, \mathbf{r_Q}$.

In this setting the equations in (2.8) and (2.9) can be written as in the below:

$$\mathbf{E^s} = \mathbf{G}\boldsymbol{\chi} \odot \mathbf{E} \tag{2.10}$$

$$\mathbf{E} = \mathbf{E^i} + \mathbf{G}\boldsymbol{\chi} \odot \mathbf{E} \tag{2.11}$$

where $\mathbf{E} = \left[\mathrm{E_x}(\mathbf{r_q}); \mathrm{E_y}(\mathbf{r_q}); \mathrm{E_z}(\mathbf{r_q})\right]_{3Q\times 1}; 1 \le q \le Q$ is the total electric field induced on the domain D, $\mathbf{E^i} = \left[\mathrm{E_x^i}(\mathbf{r_q}); \mathrm{E_y^i}(\mathbf{r_q}); \mathrm{E_z^i}(\mathbf{r_q})\right]_{3Q\times 1}; 1 \le q \le Q$ stands for the incident electric field on the sampling domain, $\boldsymbol{\chi} = \left[\chi(\mathbf{r_q}); \chi(\mathbf{r_q}); \chi(\mathbf{r_q})\right]_{3Q\times 1}; 1 \le q \le Q$ denotes the object function, $\odot$ stands for the Hadamard product and

$$\mathbf{G} = \begin{bmatrix} G_{xx}(\mathbf{r_q},\mathbf{r_p}) & G_{xy}(\mathbf{r_q},\mathbf{r_p}) & G_{xz}(\mathbf{r_q},\mathbf{r_p}) \\ G_{yx}(\mathbf{r_q},\mathbf{r_p}) & G_{yy}(\mathbf{r_q},\mathbf{r_p}) & G_{yz}(\mathbf{r_q},\mathbf{r_p}) \\ G_{zx}(\mathbf{r_q},\mathbf{r_p}) & G_{zy}(\mathbf{r_q},\mathbf{r_p}) & G_{zz}(\mathbf{r_q},\mathbf{r_p}) \end{bmatrix}_{3Q\times 3Q}; \; 1 \le q,p \le Q \tag{2.12}$$

is the matrix whose cells hold the integration of Green's function over a cubic cell. Here, the elements of Green's function matrix can be computed as given in the below [35]:

$$G_{ij} = \begin{cases} \left(\frac{4\pi a}{k^2}\left(\frac{\sin(ka)}{ka} - \cos(ka)\right)\left(\mathbf{I} + \frac{1}{k_b^2}\ \boldsymbol{\nabla\nabla}\right)\frac{\exp(ik|\mathbf{r}-\mathbf{r}'|)}{4\pi|\mathbf{r}-\mathbf{r}'|}\right)\mathbf{e}_i\mathbf{e}_j, & |\mathbf{r}-\mathbf{r}'| > a \\ \left(\frac{-1+\left(\frac{2}{3}\right)(1-ika)e^{ika}}{k^2}\right)\delta_{ij}, & |\mathbf{r}-\mathbf{r}'| < a \end{cases} \quad (2.13)$$

where $a = \sqrt[3]{\frac{3}{4\pi}}\frac{L}{N}$ is the effective radius of the cubic cell. When we take a glance on the formulation above it is obvious that solution of (2.11) requires computation of Green's matrix, whose number of elements $3Q \times 3Q$. Such a memory requirement cannot be satisfied in many commercially available computers. Besides the inversion of Green matrix requires $(3Q)^3$ operation, which is also not an acceptable time requirement. Thus to reduce the memory requirement the solution of (2.11) is performed with biconjugate gradient minimization method [35]. Thus the problem is reduced to evaluation of Green's matrix and performing matrix multiplications including **G.** To further simplify the problem matrix multiplications including Green's matrix **G** can be performed with application of fast Fourier transform (FFT) due to being Toeplitz of Green's matrix **G**. Particularly, let $\mathbf{r} = (x, y, z)$ and $\mathbf{r}' = (x', y', z')$, then:

$$\mathbf{G}(x, y, z; x', y', z') = \mathbf{G}(x - x', y - y', z - z') \quad (2.14)$$

$$[\mathbf{Gf}]_{i,j,k} = \sum_{i'=1}^{N}\sum_{j'=1}^{N}\sum_{k'=1}^{N}\mathbf{G}\left(x_i - x_{i'}, y_j - y_{j'}, z_k - z_{k'}\right)\mathbf{f}(x_{i'}, y_{j'}, z_{k'}) \quad (2.15)$$

$$[\mathbf{Gf}]_{i,j,k} = \sum_{i'=1}^{N}\sum_{j'=1}^{N}\sum_{k'=1}^{N}\mathbf{G}\left(x_{i-i'}, y_{j-j'}, z_{k-k'}\right)\mathbf{f}(x_{i'}, y_{j'}, z_{k'}) \quad (2.16)$$

$$\mathbf{Gf} = \mathrm{IFFT}_{3\mathrm{D}}\left\{\mathrm{FFT}_{3\mathrm{D}}\{\mathbf{G}\} \odot \mathrm{FFT}_{3\mathrm{D}}\{\mathbf{f}\}\right\} \quad (2.17)$$

Thus, solution of (2.11) is achieved with a biconjugate gradient fast Fourier transform (BiCG-FFT) whose overall complexity is $3Qlog(3Q)$ and whose memory comsumption is $6Q$ [35]. At the final step of forward problem, the computation of scattered field can be done by (2.10) with a canonical matrix product thanks to relatively small number of measurement points.

2.3 Inverse Scattering Problem

Inverse scattering problem is to calculate the electrical properties inside the domain D given the noisy scattered field measured on some arc $\boldsymbol{\Gamma} \in \mathbb{R}^3$**.** Here qualitative

inversion algorithms aim to reconstruct only the shapes and positions of the scatterers, i.e. $\boldsymbol{\Omega_1, \Omega_2, \dots, \Omega_P}$.

Let us consider the configuration described in the above where the measuring and illuminating antennas are located on surface $\boldsymbol{\Gamma}$, which surrounds the scattering objects $\boldsymbol{\Omega_1, \Omega_2, \dots, \Omega_P}$ and the sampling domain D. The idea behind linear sampling method is investigating the approximate solvability of near field equation, which is given by [9]:

$$\mathbf{E^s(r,y)g_{r'}(y)} = \mathbf{G(r,r')q} \tag{2.18}$$

Where $\mathbf{E^s(r,y)} = \begin{bmatrix} \mathbf{E^s_{1,1}(r,y)} & \mathbf{E^s_{1,2}(r,y)} \\ \mathbf{E^s_{2,1}(r,y)} & \mathbf{E^s_{2,2}(r,y)} \end{bmatrix}$ is the scattered electric field matrix; $\mathbf{E^s_{i,j}(r,y)}$ is the scattered electric field measured at $\mathbf{r} \in \boldsymbol{\Gamma}$ in the i[th] orthogonal direction where the illumination is made at $\mathbf{y} \in \boldsymbol{\Gamma}$ in the j[th] orthogonal direction; $\mathbf{g_{r'}(y)} = \begin{bmatrix} \mathbf{g_{r',1}(y)} \\ \mathbf{g_{r',2}(y)} \end{bmatrix}$ is the feeding coefficients to be solved; $\mathbf{G(r,r')}$ Green's tensor when a dipole at $\mathbf{r'}$ emitting in the background medium and $\mathbf{q}$ is any arbitrary polarization vector tangential to measurement surface $\boldsymbol{\Gamma}$ at measurement point **r.** In [9], it is stated that the equation in (2.10) has a finite solution only when the sampling point $\mathbf{r'}$ falls into a scatterer. Thus, reciprocal of the L^2 norm of the solution vector is an indicator for LSM:

$$\boldsymbol{W(r')} = \frac{\mathbf{1}}{\sum_{\mathbf{n}} |\mathbf{g_{r',1}(y_n)}|^2 + \sum_{\mathbf{n}} |\mathbf{g_{r',2}(y_n)}|^2} \tag{2.19}$$

Here, the equation in (2.10) is severely ill-posed and its solution requires an appropriate regularization technique [9]. In this thesis, we always apply Tikhonov regularization technique for this purpose. In Tikhonov regularization, the inversion is performed as [9]:

$$\mathbf{g_{r'}(y)} = (\boldsymbol{\alpha}\mathbf{I} + \mathbf{E^{s^*}(r,y)E^s(r,y)})^{-\mathbf{1}}(\mathbf{E^{s^*}(r,y)G(r,r')q}) \tag{2.20}$$

where $\boldsymbol{\alpha}$ is the regularization parameter. Here, the regularization parameter α can determined by imposing the following condition:

$$\frac{\sigma_N}{\alpha^2 + \sigma_N^2} \frac{\sum_{\ell=1}^{L} |\langle \mathbf{G}(\cdot, \mathbf{r}'_\ell), \mathbf{u_N}(\cdot) \rangle|}{Q} = \frac{1}{\sigma_1} \max_{1 \le \ell \le L} |\langle \mathbf{G}(\cdot, \mathbf{r}'_\ell), \mathbf{u_1}(\cdot) \rangle| \tag{2.21}$$

where $\boldsymbol{Q}$ is total number sampling points, which are $\mathbf{r'_1, r'_2, \dots, r'_L}$, $\langle \cdot, \cdot \rangle$ denotes the inner product on receiving points and $\boldsymbol{\Sigma} = \{\boldsymbol{\sigma_1, \sigma_2, \dots, \sigma_N}\}$; $\mathbf{U} = \{\mathbf{u_1, u_2, \dots, u_N}\}$ stand for the singular values, the left singular vectors of $\mathbf{E^s}$, respectively [28]. Another approach

for determination of $\boldsymbol{\alpha}$ is to fix to $\frac{\boldsymbol{\sigma_1}}{\boldsymbol{10^r}}$, where $\boldsymbol{r}$ is an arbitrary integer ranging from 2 to 5 [24].

Similarly, factorization method investigates the solvability of the following equation:

$$(\mathbf{E^{s^*}E^s})^{\frac{1}{4}}(\mathbf{r},\mathbf{y})\mathbf{g_{r'}}(\mathbf{y}) = \mathbf{G}(\mathbf{r},\mathbf{r'})\mathbf{q} \tag{2.22}$$

where $(\cdot)^*$ is the conjugate transpose and $\mathbf{F}^{\frac{1}{4}} = \mathbf{S^{-1}}\boldsymbol{\Lambda}^{\frac{1}{4}}\mathbf{S}$, where $\boldsymbol{\Lambda} = [\boldsymbol{\lambda_n}]$ is the matrix whose diagonal elements $\boldsymbol{\lambda_n}$ are eigenvalues of $\mathbf{F}$ and $\mathbf{S} = [\mathbf{S_n}]$ is the matrix whose columns $\mathbf{S_n}$ are eigenvectors of $\mathbf{F}$. In [10], it is shown that (2.12) has finite solutions if and only if the following indicator function diverges from zero:

$$\boldsymbol{W}(\mathbf{r'}) = \frac{\mathbf{1}}{\sum_{\mathbf{n}} \frac{\left|\sum_{\boldsymbol{m}} \mathbf{S_n^*}(\mathbf{r_m})\mathbf{G}(\mathbf{r_m},\mathbf{r'})\right|^2}{|\lambda_n|}} \tag{2.23}$$

3. MICROWAVE SUBSURFACE IMAGING OF OBJECTS UNDER A ROUGH AIR-SOIL INTERFACE[1]

We consider subsurface imaging of buried objects under a rough air – soil interface and present a microwave imaging method that is capable of determining the geometrical properties of multiple objects without requiring any a-priori information on the objects. The theoretical background of the method relies on factorization of scattering operators and the locations of buried objects are qualitatively determined from limited aperture near-field measurements performed with a short antenna array moving over the investigated region. The efficiency and accuracy of the method is shown with numerical results.

3.1 Introduction

Imaging of buried targets under the rough ground is a challenging inverse scattering problem with many applications in engineering. Conventional technology that uses microwaves for subsurface sensing is ground penetrating radar (GPR) which generates radargrams that require further interpretation by experts [19]. On the other hand, various inverse scattering methods have been attempted to generate more intuitive subsurface images of underground as well as providing additional information on the morphological and electrical properties of buried obstacles [14,19-24,37,41]. While the surface roughness is a critical factor that determines the limits of subsurface imaging, very few studies take surface roughness into account [25,26,31,40].

In this context, qualitative inverse scattering methods, which are almost exclusively used for reconstructing the shape of inaccessible targets from the scattered field measurements, are particularly interesting since such methods can image multiple objects without requiring a-priori knowledge [38]. Despite their attractive features

[1] This chapter is based on the paper "Akıncı, M. N., Çayören, M., 2014. Microwave subsurface imaging of buried objects under a rough air–soil interface, *Remote Sensing Letters*, 5(8), 703-712."

such as requiring fewer measurements and lower computational resources, usage of qualitative inverse scattering methods for subsurface imaging is rarely investigated [14,19-22,24,31]. This is due to the fact that these methods are not formulated depending on physical scattering mechanism that makes them obscure from engineering perspective.

In this letter, we present a qualitative imaging method for subsurface sensing. The method relies on the theoretical framework derived in [27], where the aim is to retrieve the shape of unknown dielectric objects embedded inside a dielectric body whose closed boundary and electrical parameters are known a priori. The theoretical model in [27] extensively depends on the properties of far-field operators, which are computed from far-field measurements, and requires the dielectrics to be lossless. While such restrictions seem to be incompatible with the requirements of microwave subsurface imaging, we demonstrate that the approach can be successfully adapted for subsurface sensing. To this aim, we first consider a feasible, near-field measurement configuration with a short antenna array of few elements that are distributed equidistantly with spacing Δ . The field measurements are performed above the investigated region by moving the antenna array by a distance Δ at each step. This discrete measurement configuration lets us to collect enough data that are to be measured with multiple fixed antennas in theory. Theoretical justification for near-field versions of qualitative inverse scattering methods generally depends on transforming near-field data to far field which inherently smoothen the data. Instead of using near- to far-field data transformation as described in [10], we directly use near-field data by introducing a near-field operator. We numerically verify the resulting near-field formulation and observe that the approach performs better than transforming near-field data to far field. Provided that estimate of electrical properties of soil and surface profile are known a priori, the method can inherently handle very rough surfaces due to its differential imaging mechanism. Furthermore, we demonstrate that it is possible to obtain reconstructions while the measurements are still being made.

3.2 Qualitative Imaging Applied to Subsurface Sensing

Let us confine our analysis to 2D scattering configuration depicted in Figure 3.1. Here multiple dielectric objects with various electrical properties are buried into soil, which

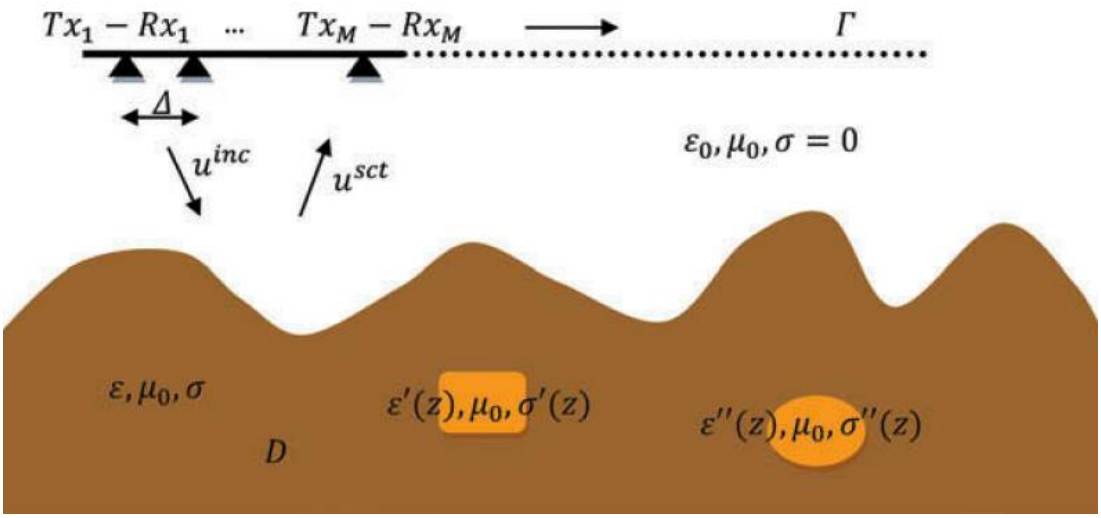

Figure 3.1 : Geometry of problem (Tx_n: n^{th} Transmitter, Rx_n: n^{th} Receiver; D: sampling domain; z:sampling point; Γ : measurement domain; ϵ_0: dielectric permittivity of vacuum; ϵ, ϵ' dielectric permittivities of soil and buried obstacles respectively; μ_0: magnetic permeability of vacuum; σ, σ' conductivities of soil and buried obstacles respectively).

is modelled with its average electrical parameters. We assume that the buried objects can be considered infinitely long in one direction and illuminated with time-harmonic microwaves that are polarized along the same direction as well. The field measurements are performed with an antenna array that moves on a planar route at a fixed height from the ground. The basic principle of the qualitative inverse scattering methods is evaluating an indicator function $w(z)$ at each point z in sampling domain, and an image is generated by plotting the variation of $w(z)$. The indicator function $w(z)$ is constructed such that its value diverges whenever sampling points fall inside an object. While selection of different indicator functions is possible, such methods exhibit certain characteristic features. In general, determination of electrical parameters such as dielectric permittivity is not the primary concern and only shapes of objects are retrieved. A recent work [27] presented a new qualitative inverse scattering method that allows us to determine shapes of multiple objects embedded inside a dielectric body with a closed surface. As noted earlier, the presented theoretical framework of [27] is not applicable to subsurface imaging in its original form and straightforward extension of similar methods to near-field case requires transforming near-field data to far field, which practically discards all advantage of near-field measurements. To adapt the theoretical framework to subsurface imaging as well as to refrain from performance degradations due to far-field conversion, let us first define a near-field operator N with a test function :

$$N\varphi = \langle \varphi | \overline{u^{sct}} \rangle_{L^2(\Gamma)} = \int_\Gamma \varphi u^{sct} d\Gamma \tag{3.1}$$

where overbar indicates complex conjugate and $\langle \cdot \mid \cdot \rangle_{L^2(\Gamma)}$ denotes the inner product defined on measurement domain Γ. In (3.1), scattered electric field $u^{sct} = u^{tot} - u^{inc}$ is the difference between total electric field u^{tot} and incident electric field u^{inc}.

Considering the near-field operator in (3.1), the indicator function w(z) can be defined as follows (Grisel et al. 2012):

$$w(z) = \left(\sum_n \frac{|\langle u_0(z,.) | \overline{\phi_n} \rangle_{L^2(\Gamma)}|^2}{\sigma_n} \right)^{-1} \tag{3.2}$$

In (3.2), u_0 denotes the total electric field inside the soil when there is no buried object. Since it is not possible to measure the field inside the soil, the total field u_0 is needed to be computed by considering the surface curvature and electrical properties of the soil. In fact, the total field values u_0 are only needed for the sampling domain that is a portion of soil where we actually search for the objects. The quantities $\{\phi_n, \sigma_n\}$ in (3.2) form the eigensystem of the operator $W_f = Re(W) + Im(W)$ with the conventions of $Re(W) = \frac{W+W^*}{2}$ and $Im(W) = \frac{W-W^*}{2i}$, where W^* denotes adjoint operator of W. The operator W is defined as:

$$W = S_0^*(N_1 - N_0) \tag{3.3}$$

Here S_0^* denotes the adjoint of operator:

$$S_0 = I + \frac{i}{4\pi} N_0 \tag{3.4}$$

where I is the unitary operator. In (3.3) and (3.4), the near-field operators $N_0\varphi = \langle \varphi | \overline{u_0^{sct}} \rangle_{L^2(\Gamma)}$ and $N_1\varphi = \langle \varphi | \overline{u_1^{sct}} \rangle_{L^2(\Gamma)}1$ are defined for the scattered fields $u_0^{sct}$and u_1^{sct}, respectively. The scattered field u_0^{sct} corresponds to the calculated field when there is no buried object and the scattered field u_1^{sct}stands for the measured field. We refer to [27] for the development of theoretical framework.

From the implementation point of view, we require three data sets that are the scattered fields u_1^{sct} and $u_0^{sct}$and the total field u_0 at each point in sampling domain. As noted earlier, $u_0^{sct}$and u_0 are required to be computed, thus a fast forward solver is needed to be integrated into the reconstruction procedure. To this aim, we utilize the buried object approach of [36], where a numerical Green's function for rough surface scattering is derived. However, since the formulations do not use Green's functions

explicitly, any other method such as finite element method can be preferred as well. For measuring the scattered field u_1^{sct} ; instead of using multi-static configurations with multiple fixed antennas, we propose to use a moving antenna array with very few elements where all antennas in array act both as transmitter and receiver similar to GPR. Let us assume that each element of the array is separated with distance Δ and there are total of M antennas as depicted in Figure 3.1. From numerical simulations, we observed a typical antenna array length of $\Delta\ (M\ -\ 1)$, which corresponds to one or two wavelengths in free space, is capable of reconstructing a complete image. We transverse the air – soil interface by shifting the antenna array with a distance of Δ at each step. If we consider discretized version of operator W in (3.3), this operation mode lets us to fill a band in the diagonal of the resulting matrix. It is obvious that the resulting matrix is a stripped version of a complete matrix that can be filled with total of N static antennas ($M << N$): By employing highly directional antennas, the length of the moving array $\Delta\ (M\ -\ 1)$ can be shortened since the field contribution due to surface outside the main lobes of antennas becomes negligible. Therefore, we can collect sufficient data to fill W without using total of N static antennas or long antenna arrays.

3.3 Numerical Validation

In this section, we present several numerical results to demonstrate the capabilities of the presented method. In all examples unless otherwise stated, operating frequency is 200 MHz and an antenna array of six line sources, which are equidistantly distributed along the free-space wavelength λ, is employed. The dry soil is modelled as a homogeneous medium having relative dielectric permittivity of $\epsilon_r\ =\ 3.6$ and conductivity of $\sigma\ =\ 10^{-5}\frac{S}{m}$ [39]. The rough surface is given with the parametric representation:

$$y(x) = \begin{cases} \frac{0.22}{\alpha}\left(\frac{x}{15}\right)^{0.3} e^{-\frac{3|x|+10x}{30}} \cos\left(\frac{\pi x}{3}\right); & x \geq 0 \\ \frac{-0.24}{\alpha}\left|\frac{x}{15}\right|^{0.3} \frac{x+3}{3} e^{-\frac{|x|}{10}} \cos\left(\frac{\pi x}{3}\right); & x < 0 \end{cases} \tag{3.5}$$

where α is used for adjusting surface roughness and (x, y) stands for the coordinate system, as depicted in Figures 3.2 and 3.3. In all cases three objects are buried into the soil, which are (i) a circular object centred at (− 3.00 m, − 3.50 m) with radius 0.50 m and with electrical parameters $\epsilon_r\ =\ 18,\ \sigma\ =\ 0.024\frac{S}{m}$, (ii) another circular object

centred at (3.00 m, −1.50 m) with radius 0.40 m and $\epsilon_r = 15,\ \sigma = 0.020\frac{S}{m}$, and (iii) an ellipse shaped object centred at (−0.20 m, −2.50 m) with radii (0.60 m, 0.85 m) and $\epsilon_r = 16.5,\ \sigma = 0.022\frac{S}{m}$. In addition to the computation of field values u_0^{sct} and u_0, the scattered field u_1^{sct}, which is to be measured with the antenna array, is synthetically generated by solving the associated forward problem via method of moments [36] and corrupted by additive Gaussian noise with an signal-to-noise ratio of 25 dB.

As we mentioned earlier, the method can reconstruct an image while field measurements are still in progress, which enables to operate in a real-time like manner. To demonstrate this capability, we consider the boundary with $= \frac{2}{7}$, where maximum peak- to-peak roughness is around 0.53 m and measurements are performed at y = 0.40 m. In all results, we plot the reconstructed $w(z)$ after normalizing with its maximum. In Figure 3.2(a), the first buried object becomes apparent when the field measurements are completed up to − 1.80 m. As the measurements progress up to 0.75 m, the second buried object becomes visible as shown in Figure 3.2(b). Finally, when the field measurements are completed for the whole surface, all three objects clearly appear as shown in Figure 3.2(c). We can conclude from Figure 3.2(a) – (c), as the number of measurements increase, quality of reconstructions improves such that the contour of shallow objects becomes distinctive. Nevertheless the reconstructions of deeper objects are still blurred even with complete measurements since the contribution of the shallow obstacles suppresses the deeper ones.

As noted earlier, conventional approach to formulate near-field counterparts of qualitative inverse scattering methods is to use a near-to-far-field transform. While we intentionally avoided this approach, to demonstrate the performance of the method in such case, we repeat the preceding numerical simulation by applying near-to-far-field transformation given in [10]. The reconstructed image is shown in Figure 3.2(d), and as expected, the performance of presented method is better with near-field data.

Another advantageous feature of the method is its ability to reconstruct objects with high dielectric contrasts, which is a challenging issue for non-linear optimization methods. To further attest the performance of the method by means of dielectric contrast, we multiply the complex dielectric permittivities of objects from deeper to shallower with factors 2, 5 and 4, respectively. The accuracy of the reconstruction that

is shown in Figure 3.2(e) is quite comparable to the case with lower dielectric contrast of Figure 3.2(c). This is, in fact, the result of the qualitative nature of the presented method. In non-linear optimization methods, an image is formed in terms of dielectric distribution of the targets that limits their efficiency with higher dielectric contrast, whereas an image in our case is formed as a plot of an indicator function w(z) that is not directly associated with the dielectric contrast.

To better understand the effect of the surface roughness on the results, we choose a very rough surface with $\alpha = 0.1$, where the maximum peak-to-peak surface roughness is about 1.50 m and measurements are made on y = 1.15 m. In Figure 3.2(f), the reconstructed buried objects are shown. While the buried objects are still distinguishable, there are clutters in the final image. To overcome such unwanted artefacts, the measurements are needed to be performed on a larger aperture. In Figure 3.2(g), the reconstruction is repeated for the measurements performed with an antenna array of 12 elements whose total length is 2λ . It is obvious that Figure 3.2(g) provides a better reconstruction at the expense of a larger measurement system. Although increase in surface roughness deteriorates the accuracy of reconstructions in subsurface imaging, the presented method provides quite successful reconstruction even with such large variations.

To further understand the capabilities of the presented method, we consider another surface given with the parametric representation:

$$y(x) = \begin{cases} \frac{11}{30} x e^{-\frac{3|x|+20x}{60}} \cos\left(\frac{\pi x}{3}\right); & x \geq 0 \\ \frac{-2}{5}|x|\left(\frac{2x+15}{15}\right) e^{-\frac{|x|}{20}} \cos\left(\frac{\pi x}{3}\right); & x < 0 \end{cases} \tag{3.6}$$

where peak-to-peak surface roughness is around 1.00 m. In this configuration, two objects are buried into the ground which are (i) a circular object centred at (− 4.00 m, − 3.50 m) with radius r = 0.50 m and with electrical parameters $\epsilon_r = 8$, $\sigma = 0.032 \frac{S}{m}$ and (ii) a square-shaped object centred at (3.50 m, − 2.00 m) with a side length ℓ = 1.00 m and with electrical parameters $\epsilon_r = 10$, $\sigma = 0.040 \frac{S}{m}$. First, we investigate the effects of different operating frequencies. In Figure 3.3(a) – (c), reconstructed images are shown for frequencies 400, 300 and 200 MHz, respectively. It is obvious that deeper objects become less apparent as operating frequency increases while

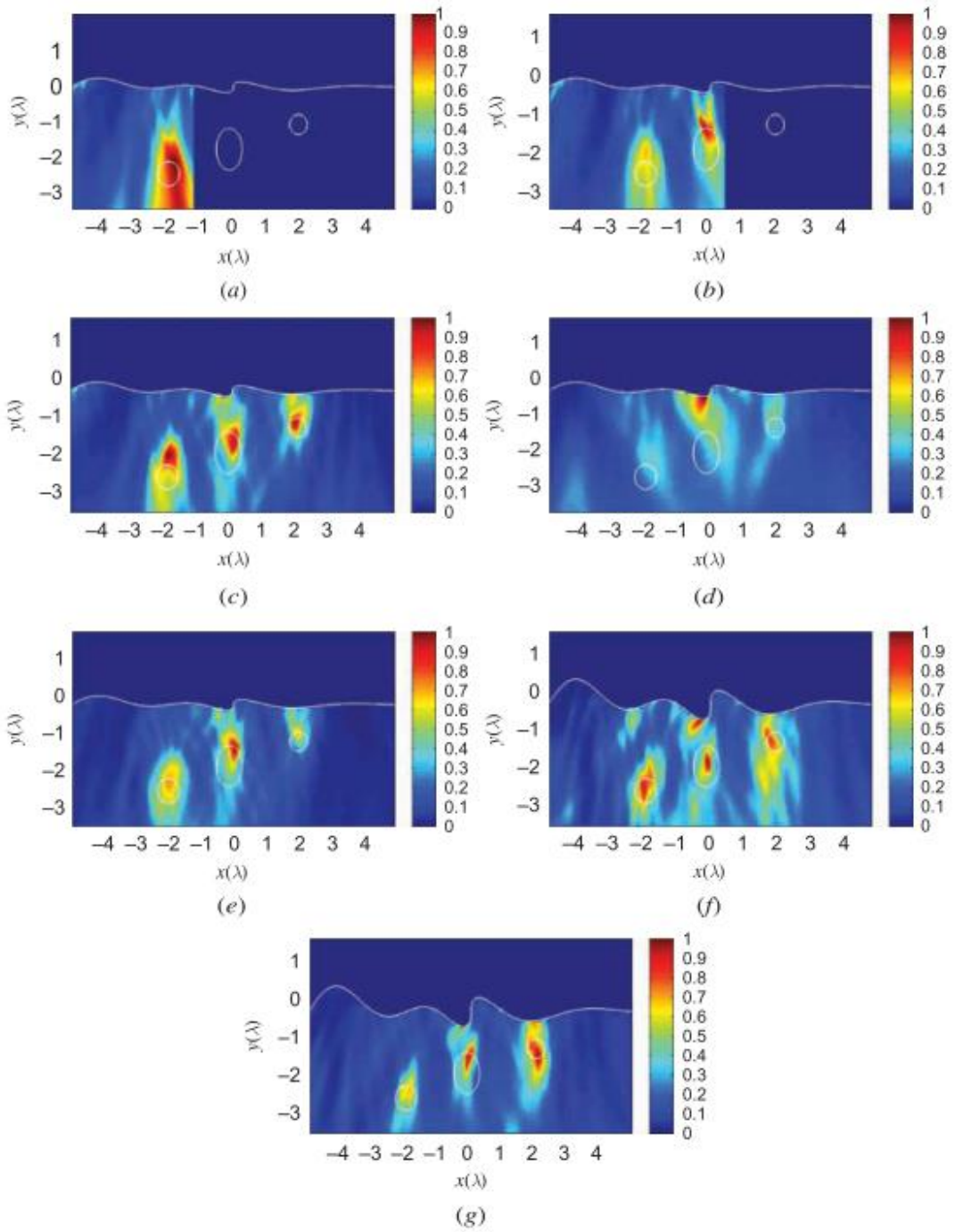

Figure 3.2 : Values of $\frac{w(z)}{\max(w(z))}$ for reconstructed subsurface images: (a) when measurements are completed upto − 1.80 m; (b) when measurements are completed upto 0.75 m; (c) when completed for whole surface; (d) when near-to-far-field transform is applied to near-field measurements; (e) for higher dielectric contrast among objects; (f) for very rough surface case with 6 antennas with an equal spacing of $\frac{\lambda}{6}$ and (g) for very rough surface case with 12 antennas with an equal spacing of $\frac{\lambda}{6}$. The coordinates shown are measured in terms of λ.

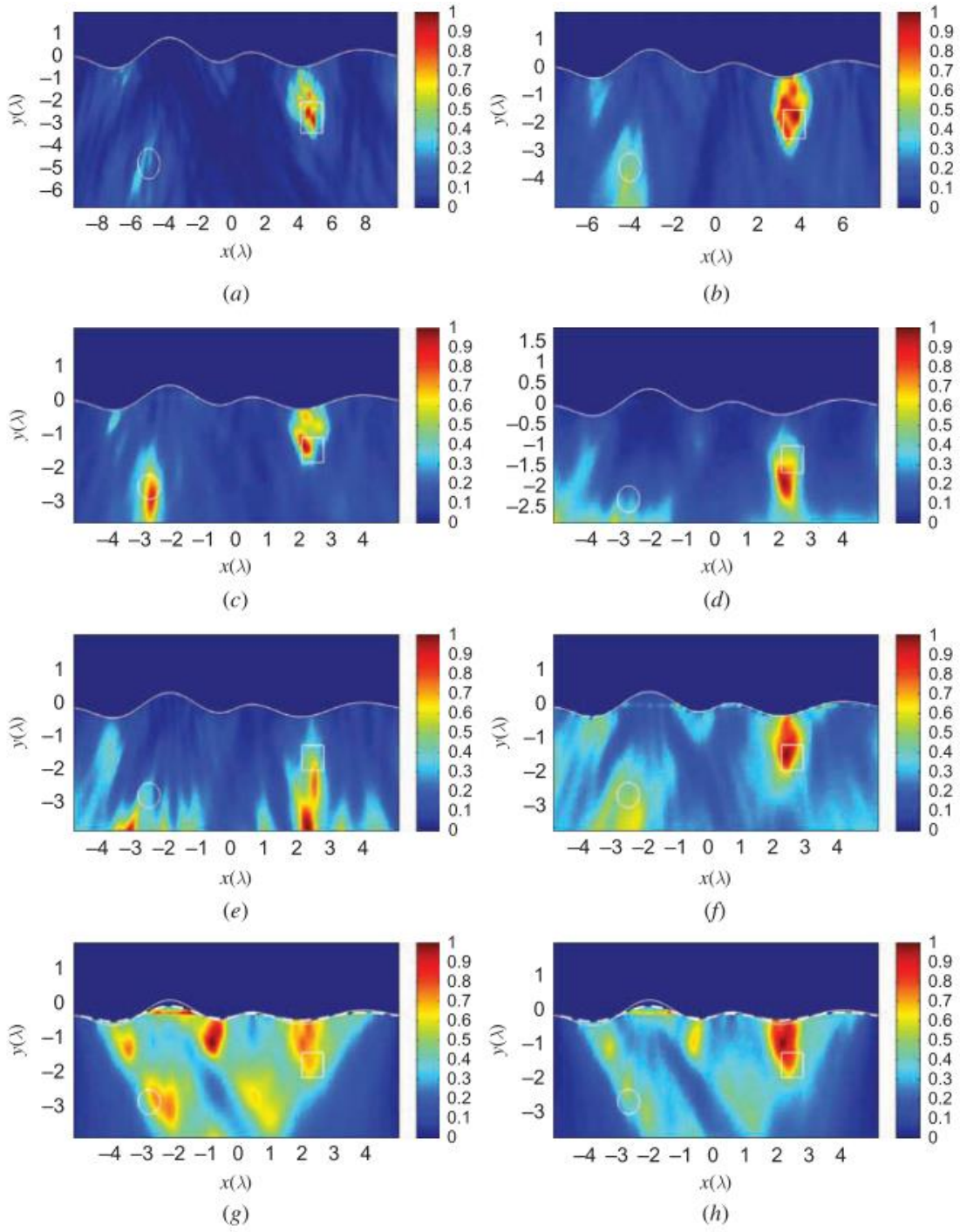

Figure 3.3 : Values of $\frac{w(z)}{\max(w(z))}$ for reconstructed subsurface images for (a) dry soil at 400 MHz, (b) dry soil at 300 MHz, (c) dry soil at 200 MHz, (d) soil with 5% moisture at 200 MHz, (e) soil with 10% moisture at 200 MHz, (f) randomly varying electrical parameters of soil at 200 MHz, (g) wrongly estimated surface case (dashed: wrongly estimated surface, solid: exact profile) and (h) wrongly estimated surface case with 12 antennas with an equal spacing of $\frac{\lambda}{6}$ (dashed: wronglyestimated surface, solid: exact profile).

reconstructed images get sharper. This is in fact the result of the well-known trade-off between skin depth and spatial resolution such that microwaves can penetrate deeper into soil as the operating frequency decreases, which in turn degrades spatial resolution. Besides, increase in conductivity exponentially reduces penetration of microwaves into soil, and the main factor that contributes to conductivity of soil is moisture content. To reveal outcomes of increased moisture content to the presented method, we consider soils with 5% and 10% moisture contents. In these case, electrical properties of soils are $\epsilon_r = 5, \sigma = 0.001 \frac{S}{m}$ for 5% and $\epsilon_r = 7, \sigma = 0.002 \frac{S}{m}$ for 10% moisture content [39]. In Figure 3.3(d) and (e), reconstructed images are shown for moisture contents 5% and 10%, respectively. If we compare results depicted in Figure 3.3(c) – (e), increasing moisture content severely degrades reconstructions such that deeper objects become non-distinguishable. This is a combined result of two effects: first, increase in soil conductivity reduces the penetration of microwaves into soil as mentioned earlier; second, with increasing moisture, the effective dielectric permittivity of soil increases, which in turn lowers dielectric contrast between the objects and the soil. As a consequence of low contrast, scattered field from the buried objects gets weaker, which makes the objects hard to distinguish from the soil.

We formulate the presented method depending on effective electrical properties of soil, but in reality determination of effective electrical properties of soil may not be straightforward. To stress the fact that the formulation does not require such strict a-priori information, we consider an example where electrical properties of soil change randomly. To this aim, we added separate random variations to both relative dielectric permittivity and conductivity of soil in the form of $\tilde{\epsilon_r} = (1 + \alpha)\epsilon_r$ and $\tilde{\sigma} = (1 + \beta)\sigma$; respectively. Here $\alpha, \beta \in [0,1)$ are uniformly distributed random variables. As shown in Figure 3.3(f), the square-shaped object is apparent while the deeper circular object is no longer visible. This is indeed the result of two main factors: first, there is high level of variation in electrical properties, and second, the effective electrical parameters used in simulation are not valid anymore due non-zero mean of randomness.

Up to this point, we assume that the surface curvature is known. To attest performance of the presented method when the surface profile is wrongly estimated, we consider a deformed surface:

$$\tilde{y}(x) = 0.6y(x) - 0.01\cos\left(\frac{\pi x}{3}\right); \qquad -7.5m \leq x \leq 7.5m \tag{3.7}$$

where y (x) is the exact surface profile given by (3.6). The reconstructed subsurface image is shown in Figure 3.3(g). By comparing against Figure 3.3(c), we infer that errors in surface profile cause large artefacts. This is mainly due to fact that wrongly estimated surface profile results large deviations in total field on the sampling domain which may induce large indicator function values where there is no objects. For alleviating deterioration in the image, we repeat the same simulation with an antenna array of 12 elements equidistantly distributed along the length of 2λ . From the reconstructed image shown in Figure 3.3(h), we can conclude that using a large array suppresses artefacts, but it might not be enough to capture sufficient information for deeper objects. In fact, Figure 3.3(g) and (h) demonstrates a very general characteristic of microwave subsurface imaging, such that the exact knowledge of surface profile is a critical factor that determines both accuracy and reliability of the reconstructions. When the estimated surface profile deviates from the exact surface, the field contribution due to these deviations corrupts the scattered field from the buried objects. Thus variation of surface profile is needed to be known accurately and only very slight deviations can be tolerated.

3.4 Conclusions and Future Work

We present a microwave imaging method for detecting and localizing buried objects under a rough air – soil interface. The formulation depends on factorization of scattering operators where locations of objects are qualitatively determined as the norm of an indicator function diverges. The method is capable to reconstruct locations of multiple targets from a limited aperture, near-field measurements that are performed with a short antenna array moving over the soil. In addition to an estimate of effective electrical parameters of soil in which the method can tolerate certain degree of randomness, the surface curvature is needed to be known a priori. Other than that, there are no limitations on electrical properties of buried targets such that lossy dielectric materials even with high dielectric contrasts among them can be handled accurately. Numerical simulations reveal that the method can perform in a real-time-like operation mode where reconstructed image is updated while measurements are still in progress. Another capability of the method is its ability to handle very rough surfaces. Further

research will be towards extending the method to 3D electromagnetic case and validating against experimental measurements.

4. QUALITATIVE MICROWAVE IMAGING WITH SCATTERING PARAMETERS MEASUREMENTS[2]

Microwave imaging (MWI) systems extensively employ vector network analyzers for microwave measurements due to their high availability and accuracy. This is in contrast to theoretical models, which are naturally formulated in terms of scattered electric field vectors. Accordingly, experimental verification of MWI methods requires an intermediate step where measured scattering parameters are converted to scattered electric fields. In parallel to recent researches, we develop formulations of two closely related qualitative inverse scattering methods—the linear sampling method and the factorization method—directly in terms of scattering parameters to avoid the intermediate conversion step. To this aim, we introduce vector S-parameters and we extend the vector Green's function for S-parameters to the dyadic case. There are certain advantages of these formulations. First, the formulations incorporate the antenna radiation characteristics. Moreover, they reduce the measurement time since they do not require any pre- or post-measurement process. Experimental results show that the proposed methodologies can accurately reconstruct the shape of the targets.

4.1 Introduction

Microwave imaging (MWI) emerges as a novel technology that aims to extract physical properties of inaccessible objects from scattered electric field measurements at the microwave frequency range. These imaging approaches have prominent applications in nondestructive testing (NDT) and especially in medical imaging where microwaves are quite attractive due to their non-ionizing nature when interacting with biological tissues [30].

---

[2] This chapter is based on the paper "Akıncı, M. N., Çağlayan, T., Özgür, S., Alkaşı, U., Ahmadzay, H., Abbak, M., Çayören M., Akduman, İ., 2015. Qualitative microwave imaging with scattering parameters measurements, *IEEE Transactions on Microwave Theory and Techniques*, 63(9), 2730-2740"

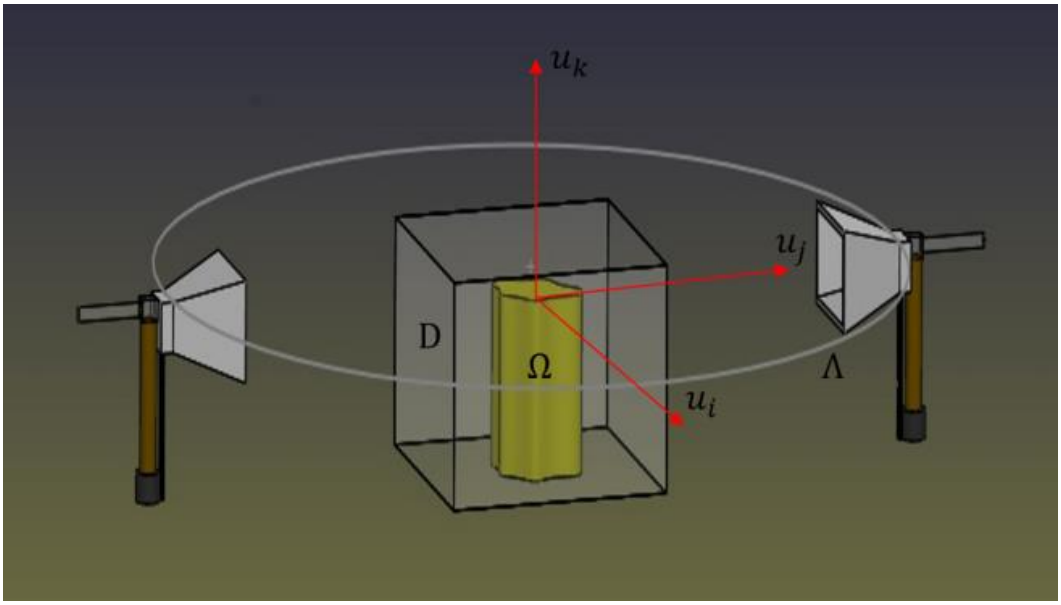

Figure 4.1 : Problem geometry (D: Sampling domain, Ω: Support of all scatterers, Λ: Illumination-measurement domain, $\mathbf{u_i}$, $\mathbf{u_j}$, $\mathbf{u_k}$: A right handed coordinate system)

MWI systems extensively incorporate vector network analyzers (VNAs) instead of implementing additional modules to perform microwave measurements. This is particularly driven by the availability of high-performance VNAs. While there are alternative ways of reconstructing an image in MWI, imaging methods are naturally formulated in terms of scattered electric field vectors, whereas measured scattering parameters (S-parameters) are only auxiliary quantities. Consequently, an intermediate step is required for experimental setups where measured S-parameters are mapped to scattered electric fields. This is mostly handled by comparing simulated electric fields against measured S-parameters [28,29,42]. In particular, we also utilize from the canonical S-parameters—electric fields' conversion method given in [29] for experimentally comparing the electric field-based formulations of qualitative imaging methods [43].

Inverse scattering theory provides a group of highly theoretical approaches known as qualitative imaging methods [8]. These methods are based on inverting an integral equation for each point over a reconstruction domain to determine the shape and position of unknown scatterers without requiring any a priori information. Comparing with nonlinear optimization methods [1]–[5], which model the physical scattering mechanism to determine electrical properties of dielectric objects, qualitative inverse scattering methods are generally easier to implement and more efficient in use of computational resources. Despite their attractive features, such methods are not

frequently used in engineering applications due to their mathematical background [28,29,44,45]. Two well-known representatives of qualitative inverse scattering methods are: 1) the linear sampling method (LSM) [9] and 2) the factorization method (FM) [16]. These two methods are in fact quite similar in formulation as well as in performance [11]–[14].

As a better alternative to the calibration step between the S-parameters and the electric fields, recent studies demonstrated that measured S-parameters can be effectively modeled with vector spherical wave functions [46]. Besides, the Born iterative method can be directly formulated in terms of S-parameters, by defining integral equations comprised of a vector Green's function for S-parameters [47]. In this direction, we consider LSM and FM to develop novel formulations of their S-parameter counterparts. For this purpose, we introduce two novel notions: vector S-parameters and the dyadic Green's function for S-parameters, where the second is the generalization of the vector Green's function given in [46]. Such formulations are quite important from an engineering perspective for two main reasons. First, antenna radiation characteristics are inherently incorporated into the solution procedure without any simplification. Second, measured S-parameters can be directly applied to the imaging methods as input without any preprocessing, which spares the measurement time associated with the calibration. The developed theoretical models are experimentally verified with scattering parameters measured inside an anechoic chamber. Reconstructions, which are obtained directly from measurements, indicate the accuracy and stability of the proposed formulations. Moreover, the effectiveness of incorporating multi-frequency measurements is demonstrated experimentally. Note that this work is different from the authors recent study in [43], which performs an experimental comparison of the electric-field-based LSM and FM, as indicated above.

This paper is organized as follows. In Section II, we briefly outline the canonical formulations of the LSM and FM to stress the analogy between electric-field-based and S-parameter-based microwave scattering mechanisms. In Section III, the novel formulations of S-parameter-based LSM and FM are then explained in detail. Later, in Section IV, we present several reconstructions that are achieved with the proposed formulations. Throughout this paper, time convention is assumed and suppressed.

4.2 Qualitative Microwave Imaging

Qualitative inverse scattering methods attempt to reconstruct the shape of inaccessible targets from scattered fields without making any assumptions on the number of targets or their electrical properties. These methods have been successfully applied in various subjects such as: NDT [48], medical imaging [32]–[34], or subsurface imaging [14,31,49,50]. Two closely related representatives of such formulations are the LSM and the FM. Here we first briefly introduce the LSM and FM to further develop formulations based on S-parameters.

Let us consider a 3-D electromagnetic scattering mechanism from arbitrary dielectrics in free space, as depicted in Figure 4.1. It is well known that scattered electric field is governed by the data equation:

$$\mathbf{E^{sct}}(r) = \int_{\Omega} \mathbf{G}(r, r')\chi(r')\mathbf{E^{tot}}(r')dr' ; \;\; r' \in \Omega, r \in \mathbb{R}^3 \tag{4.1}$$

where Ω is the total volume of all corresponding objects. Here, $\mathbf{G}(r, r')$ is the dyadic Green's function given by:

$$\mathbf{G}(r, r') = \left(\mathbf{I} + \frac{1}{k_0^2}\nabla\nabla\right)\frac{\exp(ik_0|r-r'|)}{4\pi|r-r'|} \tag{4.2}$$

where k_0 is the complex wavenumber of the medium and $\chi(r') = k^2(r') - k_0^2$ is the so-called object function. The electric field is determined by inverting the object equation, which is:

$$\mathbf{E^{tot}}(r) = \mathbf{E^{inc}}(r) + \int_{D} \mathbf{G}(r, r')\chi(r')\mathbf{E^{tot}}(r')dr' ; \;\; r', r \in \Omega \tag{4.3}$$

where $\mathbf{E^{inc}}(r)$ stands for the incident electric field. In this setting, let us define the near-field operator $F(\cdot)$ and the near-field equation as [9]:

$$(F\phi_z)(x) \coloneqq \int_{\Lambda} \boldsymbol{\nu}(x) \times \mathbf{E^{sct}}\big(x, y, \phi_z(y)\big)dy$$

$$= \boldsymbol{\nu}(x) \times \mathbf{G}(x, z)\mathbf{q}; \qquad x, y \in \Lambda; \mathrm{z} \in \mathrm{D}; \mathbf{q} \in \mathbb{R}^3 \tag{4.4}$$

In (4.4), for arbitrary polarization, $\mathbf{q}$, *x*, and, *y* denote source and observation positions, respectively, *z* stands for a point in the sampling domain D, $\boldsymbol{\nu}$ is the unit normal vector defined on the observation surface Λ, and ϕ_z stands for the test function on which operates. As proven in [9], the main condition of the LSM is:

$$z \notin \Omega \wedge (F\phi_z) \rightarrow \boldsymbol{\nu} \times \mathbf{G}(\cdot, z)\mathbf{q} \Rightarrow \big||\phi_z|\big|^{-1}_{L^2(\Lambda)} \rightarrow 0 \tag{4.5}$$

where $\left|\left|\cdot\right|\right|_{L^2(\Lambda)}$stands for the Euclidian norm for the Hilbert space defined on the surface Λ:

$$\left|\left|f\right|\right|_{L^2(\Lambda)} = \int_\Lambda |f|^2 d\Lambda \tag{4.6}$$

This condition can be interpreted as: provided that a sampling point z falls inside an object Ω, there exists a function ϕ_z that satisfies the near field equation (4.4) such that the indicator function $W(z) \coloneqq \left|\left|\phi_z\right|\right|^{-1}_{L^2(\Lambda)}$ becomes greater than zero. Here, the proposal in (4.5) is proven to be true, but $z \in \Omega$ does not always imply that $W(z) > 0$, i.e., there can be some regularization schemes which can come up with a non-finite solution of (4.4) [9]. Therefore, all scatterers can be reconstructed by plotting the indicator function $W(z)$ on the entire sampling domain D. (It is assumed that the sampling domain D completely encapsulates the scatterers Ω.) For this goal, the ill-posed near field equation in (4.4) must be inverted via Tikhonov regularization [9]. The choice of the regularization parameter has a great influence on the quality of the obtained images and choosing optimal parameter for each sampling point requires an estimate of noise power, which may not be available in real measurement systems [44]. Apart from that, the computation of an optimal parameter for each sampling point is the most time consuming part of LSM [44]. No-sampling version of LSM in [51,52] and regularization routine in [28] are a few solutions to these limitations.

Similarly, as proven in [11,16,53], the main condition of FM is:

$$z \notin \Omega \wedge \mathbf{\nu} \times \mathbf{G}(\cdot, z)\mathbf{q} \notin R\left((F^* F)^{\frac{1}{4}}\right) \Leftrightarrow$$

$$W(z) \coloneqq \left(\sum_l \frac{|\langle \mathbf{\nu} \times \mathbf{G}(\cdot, z)\mathbf{q}, \psi_l \rangle_{L^2(\Lambda)}|^2}{|\lambda_l|}\right)^{-1} \to 0 \tag{4.7}$$

where $(\cdot)^*$ denotes the conjugation operator, $R(\cdot)$ denotes the range of related operator, $\{\lambda_l, \psi_l\}$ is the eigensystem of F and $\langle \cdot, \cdot \rangle_{L^2(\Lambda)}$ denotes the inner product for the Hilbert space defined on the surface Λ, which is given by:

$$\langle f, g \rangle_{L^2(\Lambda)} = \int_\Lambda f g^* d\Lambda \tag{4.8}$$

Eventually, whenever a sampling point z falls inside an object and $\mathbf{\nu} \times \mathbf{G}(\cdot, z)\mathbf{q}$ belongs to the range of the operator $(F^* F)^{\frac{1}{4}}$ (i.e., $(F^* F)^{\frac{1}{4}} \phi_z = \mathbf{\nu} \times \mathbf{G}(\cdot, z)\mathbf{q}$ has a solution) then the indicator function given in (4.7) becomes greater than zero. Plotting

the indicator function over the entire sampling domain reveals the objects in a similar fashion. Note that, in contrast to LSM, FM fully characterizes the sampling points as stressed in (4.7) [16]. Nonetheless as stated in [9], LSM is shown to be applicable to a wide range of problems, whereas generalization of FM is a more challenging issue. For further discussion of the theoretical aspects of the LSM and FM, we refer to monographs [9,16] and physical interpretations of the methods can be found in [45,54].

Although the above formulations are for a monochromatic case, multi-frequency measurements must be carried out to obtain better image reconstruction. Both LSM and FM can be easily adapted to the multi-frequency case, since they only aim to recover the shape instead of the frequency dependent dielectric parameters of the target. For more detailed discussions about multi-frequency techniques we propose the reader to see [14,55–58].

4.3 Formulating LSM and FM in terms of Scattering Parameters

There are certain practical issues in the above theoretical model if an experimental configuration is considered. First, the scattered electric field vector $\mathbf{E}^{\mathbf{sct}}$ and incident electric field vector $\mathbf{E}^{\mathbf{inc}}$ must be measured over the measurement domain Λ for all tangential polarizations. It is obvious from (4.4) that measuring only amplitude of the electric field is not sufficient and phase must be measured accurately as well. Furthermore, multiple antennas are utilized in microwave measurement setups for both exciting and sensing electromagnetic fields thus their radiation characteristics become an integral part of the measurement systems. While in practice, antennas are generally approximated as analytical sources such as line/point sources or Gaussian beams, this is in fact an oversimplification of the actual case. Therefore, a generic antenna characterization method must be included in reconstruction procedures. Among all practical considerations, the actual measurement device is the most important factor. Real-world microwave measurement systems exclusively use laboratory grade VNAs due to their accuracy as well as commercial availability. This leads to measuring S-parameters instead of electric field values for a fixed polarization. In this context, if we consider using either LSM or FM in practice, we need to map the measured S parameters to the scattered electric field $\mathbf{E}^{\mathbf{sct}}$ in (4.4). Conventional techniques are to apply calibrations, which simply find coefficients by comparing simulated electric

fields and measured S-parameters for canonical objects such as spheres or long cylinders [28,29,42,44,45].

4.3.1 Incorporating antenna radiation characteristics

Recent research proposed an elegant way to tackle such restrictions by representing S-parameters with spherical wave functions [46,47,59]. To this aim, the incident field $\mathbf{E^{inc}}$ is first expanded into series of divergenceless spherical vector wave functions as [46,47,59]:

$$\mathbf{E^{inc}}(r) = \sum_{p=1}^{\infty}\sum_{k=-p}^{p} \alpha_{pk}\mathbf{M_{pk}}(r) + \beta_{pk}\mathbf{N_{pk}}(r)\,, \quad r \in \mathbb{R}^3;\ \alpha_{pk}, \beta_{pk} \in \mathbb{C} \quad (4.9)$$

where $\mathbf{M_{pk}}$, $\mathbf{N_{pk}}$ are spherical harmonics [2]. This representation allows simulating models of real antennas in 3D electromagnetic solvers. The unknown coefficients α_{pk} and β_{pk} are determined by inverting (4.9) using simulated electric fields $\mathbf{E^{inc}}$ over a sphere enclosing the antenna. In fact, inversion of (4.9) is an ill-posed problem and an approximate but stable solution can only be achieved in a least square sense by using a form of regularization such as Tikhonov inversion [47]. Once the unknown coefficients are determined, the incident electric field from the antenna can be evaluated in whole space. At this stage, we propose a simple strategy for optimal selection of the total number of harmonics. Let us assume that the electric fields $\mathbf{E_1^{inc}}$ and $\mathbf{E_2^{inc}}$correspond to simulated field values over two concentric spheres enclosing the antenna model. Then the coefficients in (4.9) are determined in a least square sense by inverting $\mathbf{E_1^{inc}}$. With these coefficients, the electric field $\widetilde{\mathbf{E_2^{inc}}}$ can be evaluated on the same sphere where the $\mathbf{E_2^{inc}}$ was simulated previously. The optimal number of harmonics is determined as the minimum number of harmonics for which the error norm $\frac{\left|\left|\mathbf{E_2^{inc}} - \widetilde{\mathbf{E_2^{inc}}}\right|\right|}{||\mathbf{E_2^{inc}}||}$ becomes lower than an arbitrarily selected threshold τ.

Let us define a normalized incident field $\mathbf{e^{inc}}$ [46]:

$$\mathbf{e^{inc}} = \frac{\mathbf{E^{inc}}}{\sqrt{2P_{ave}Z_0}} \quad (4.10)$$

where P_{ave} is the average input power and Z_0 is the input impedance of the antenna. With the normalization in (4.10), the object equation for the electric field given by (4.3) becomes [46]:

$$\mathbf{e^{tot}}(x_m, y_n) = \mathbf{e^{inc}}(x_m, y_n) + \int_D \mathbf{G}(y_n, z)\chi(z)\mathbf{e^{tot}}(z)dz\,;\ \ x_m, y_n \in \Lambda, \mathrm{z} \in \Omega \quad (4.11)$$

Here x_m and y_n denote the positions of m[th] transmitting antenna and n[th] receiving antenna, respectively. In parallel to the definition of the scattered electric field, scattered S-parameters $S_{n,m}^{sct}$ are defined as a difference between measured S-parameters $S_{n,m}^{tot}$ when the objects are present and $S_{n,m}^{inc}$ when there are only antennas [46]:

$$S_{n,m}^{sct} = S_{n,m}^{tot} - S_{n,m}^{inc} \tag{4.12}$$

Based on the field expansion in (4.9) and the normalization in (4.10), it is proved that scattered S-parameters can be expressed as [46]:

$$S_{mn}^{sct} = \int_D \mathbf{g}(y_n, z)\chi(z)\mathbf{e^{tot}}(z)dz\,;\;\; x_m, y_n \in \Lambda, \mathrm{z} \in \Omega \tag{4.13}$$

where $g(y_n, z)$ is the so-called vector Green's function:

$$\mathbf{g}(y_n, z) = \frac{iZ_0}{2\omega\mu}\mathbf{e^{inc}}(y_n, z);\quad z \in \mathbb{R}^3, y_n \in \Lambda \tag{4.14}$$

The equations expressed in (4.11) and (4.13) are valid under two assumptions: first, there is no incoming field in the frame of the transmitting antenna and there is no outgoing field in the coordinates of the receiving antenna; second, there is no multiple scattering between any two antennas, antennas and objects [59]. Although these assumptions seem to be restrictive at first glance, such representation is demonstrated to be useful in practical cases [46,47]. Interested reader can find the validations and a comprehensive analysis of (4.9), (4.13) in [46,47,59].

4.3.2 Vector S-parameters based formulations of LSM and FM

A careful examination of (4.1), (4.3) and their S-parameter counterparts (4.11), (4.13) reveals that there is a direct analogy between scattered electric field and measured S-parameters for a specific polarization. To further emphasize this analogy, let us introduce the vector form of scattered S-parameters as:

$$\mathbf{S}^{sct} = S_i^{sct}\mathbf{u_i} + S_j^{sct}\mathbf{u_j} + S_k^{sct}\mathbf{u_k} \tag{4.15}$$

where (S_i^{sct}, S_j^{sct}, S_k^{sct}) are scattered S-parameters for orthogonal polarizations ($\mathbf{u_i}$, $\mathbf{u_j}$, $\mathbf{u_k}$). With this new definiton of S-parameters, (4.13) becomes:

$$\mathbf{S}_{mn}^{sct} = \int_D \mathbf{G_s}(y_n, z)\chi(z)\mathbf{e^{tot}}(z)dz\,;\;\; x_m, y_n \in \Lambda, \mathrm{z} \in \Omega \tag{4.16}$$

where $\mathbf{G_s}$ is the dyadic Green's function for S-parameters given by:

$$\mathbf{G_s} = \frac{iZ_0}{2\omega\mu}\sum_{m\in(i,j,k)}\sum_{n\in(i,j,k)} e_{mn}^{inc}\,\mathbf{u_m}\mathbf{u_n} \tag{4.17}$$

In (4.17), e_{mn}^{inc} is the $\mathbf{u_n}$ component of normalized incident electric field produced by a $\mathbf{u_m}$ polarized antenna. While not formally defined, $\mathbf{G_s}$ in (4.17) acts as a Green's function in a sense that it generates measured S-parameters for arbitrary antennas. Then making use of the obvious analogy between (4.1), (4.3) and (4.11), (4.16) we can define a new near field operator:

$$(L\phi_z)(x) \coloneqq \int_\Lambda \boldsymbol{\nu}(x) \times \mathbf{S^{sct}}\big(x, y, \phi_z(y)\big)dy \quad x, y \in \Lambda; \mathrm{z} \in \mathrm{D}; \tag{4.18}$$

which is the S-parameter complement of the near field operator in (4.4). Thereby, the main condition of LSM for S-parameters can be written as:

$$z \notin \Omega \wedge (L\phi_z) \to \boldsymbol{\nu} \times \mathbf{G_s}(\cdot, z)\mathbf{q} \Rightarrow \big|\big|\phi_z\big|\big|_{L^2(\Lambda)}^{-1} \to 0 \tag{4.19}$$

As in the case of traditional LSM, the shape of all scatterers can be obtained by plotting the indicator function $W(z)$ after inverting the ill-conditioned near field equation (4.19) by means of Tikhonov regularization. Although it is not formally shown to be an optimal solution, this paper exploits the regularization procedure in [28] due to its simplicity and effectiveness.

In a similar way to LSM, the condition for FM with S-parameters becomes:

$$z \notin \Omega \wedge \boldsymbol{\nu} \times \mathbf{G}(\cdot, z)\mathbf{q} \notin R\left((L^*L)^{\frac{1}{4}}\right) \Leftrightarrow$$

$$W(z) \coloneqq \left(\sum_l \frac{|\langle \boldsymbol{\nu}\times\mathbf{G_s}(\cdot,z)\mathbf{q}, \psi_l\rangle_{L^2(\Lambda)}|^2}{|\lambda_l|}\right)^{-1} \to 0 \tag{4.20}$$

where $\{\lambda_l, \psi_l\}$ is the eigensystem of L.

The conditions in (4.19), (4.20) inherently take antennas into account, which is an important aspect of the developed formulations. Arbitrary antennas such as corrugated horn antennas or Vivaldi antennas, which are extensively used in MWI systems, can be accurately incorporated into the solution procedure without any simplification. Furthermore, as a consequence of the newly introduced near field operator in (4.18), the measured S-parameters are directly included in the solution methodologies without requiring to be converted into electric field. Despite the affinity between electric field based formulations of (4.5), (4.7) and S-parameters based formulations of (4.19), (4.20) these conditions differ radically. The main difference is the dyadic Green's

function for S-parameters $\mathbf{G_s}$ in (4.17) is heavily dependent on antenna radiation characteristics, whereas the canonical Green's function $\mathbf{G}$ in (4.2) is independent of excitation.

Finally, note that the derived algorithms can also be modified for multi-frequency measurement scenarios in a similar way to electric field based formulations. Here for simplicity we prefer integrating over all available frequencies [55]:

$$W(z) = \int_{f_{min}}^{f_{max}} W(z,f)df \tag{4.21}$$

where $W(z,f)$ stands for the indicator function for a single frequency, which is defined in (4.19) or (4.20). Through the measurements, it is observed that even such a simple summation operation for incorporating multi-frequency data dramatically increases the quality of the results.

4.3.3 Implementation for cylindrical microwave scanners

Cylindrical scanning for MWI systems is a common configuration due to its simplicity [60,61]. Here we discuss the discretization of the presented formulations for such mechanisms.

For implementing LSM, surface normal and polarization vectors are explicitly selected as $\boldsymbol{\nu} = \mathbf{a_\rho}$ and $= \mathbf{a_z}$, respectively; where $(\mathbf{a_\rho}, \mathbf{a_\theta}, \mathbf{a_z})$ is the well-known basis of cylindrical coordinates [2]. Then, by discretizing the sampling domain into M cuboid cells centered around points $z_1, z_2, .., z_M$ near field equation in (4.19) can be written as:

$$\mathbf{L}\phi = \mathbf{U} \tag{4.22}$$

Here $\mathbf{L} = [L_{m,n}] = [S^{sct}_{n,m} R\Delta\theta\Delta z]$, where $S^{sct}_{n,m}$ denotes the z component of the scattered vector S-parameter, $R\Delta\theta\Delta z$ is the Jacobian resulting from the integration and $m, n \in 1, 2, \ldots, N$ denote the numbers associated with transmitting and receiving antennas respectively. In (4.22), $U = \left[U_{n,k}\right] = \left[\mathbf{e^{inc}_{z_k,n}}.\mathbf{a_z}\right]; k \in 1, 2, \ldots, M, n \in 1, 2, \ldots, N$ is the matrix whose entries are the $\mathbf{a_z}$ component of the normalized incident field produced by the receiving antenna while illuminating the sampling domain. Then, this equation is solved as explained in [9] and the indicator function is computed as:

$$W(z_k) = \left|\left|\phi_{z_k}\right|\right|^{-1}_{L^2(\Lambda)} = \left(\sum_{n=1}^{N} |\phi_{z_k,n}|^2 R\Delta\theta\right)^{-1}; \quad k \in 1,2,\ldots,M \tag{4.23}$$

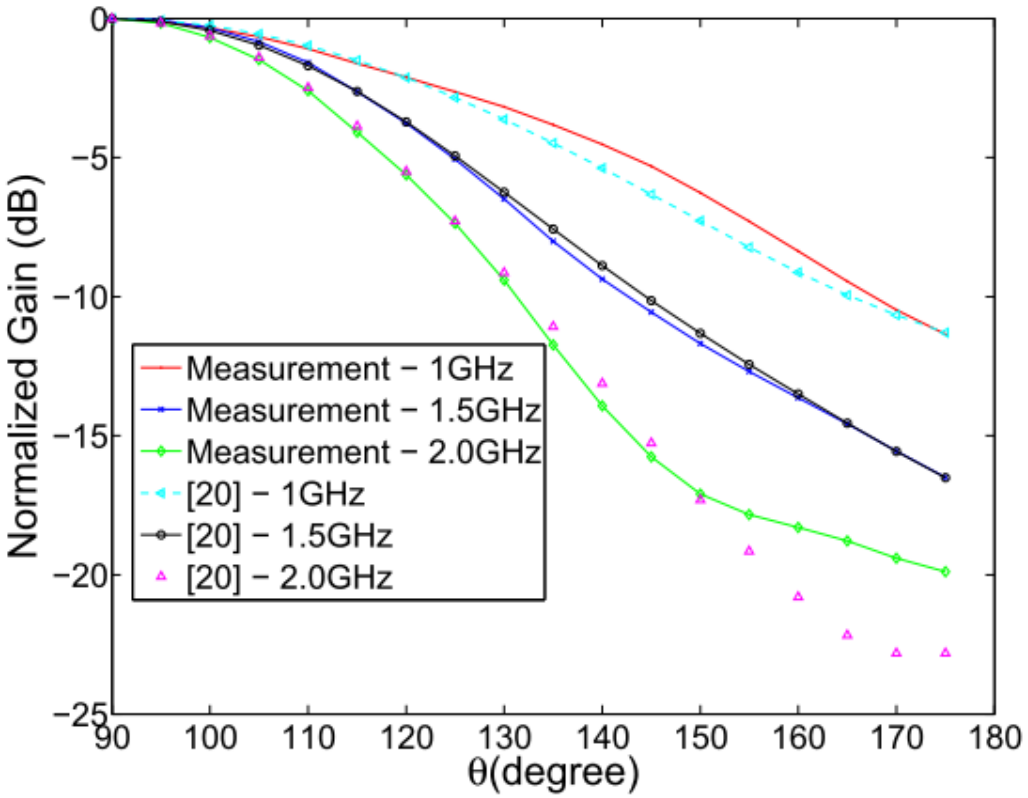

Figure 4.2 : Measured - Computed normalized gain of the ridged horn antenna at $R = 0.85\,m$, $\varphi = 0°$ and $90° < \theta < 180°$ where x, y and z denote the canonical Cartesian coordinates. The major lobe of the antenna is directed towards x-axis. (Spherical coordinates are defined as: $R = \sqrt{x^2 + y^2 + z^2}$, $\theta = \cos^{-1}\left(\frac{z}{R}\right)$ and $\theta = \tan^{-1}\left(\frac{y}{x}\right)$. When computing the normalized gain the representations in (9) and (10) are employed. Here the coefficients α_{pk}, β_{pk} are calculated from the simulated electric fields on the sphere having a radius of $R = 0.725\,m$. Mean square errors between the measured and computed values are 4.58%, 1.72% and 3.63% for 1.0 GHz, 1.5 GHz and 2.0 GHz, respectively.)

Similarly, for implementation of FM, using the same notation conventions, the indicator function is evaluated as:

$$W(z_k) = \left[\sum_{n=1}^{N} \frac{|\langle U_k, \psi_n \rangle_{L^2(\Lambda)}|^2}{|\lambda_n|}\right]^{-1}; \quad k \in 1,2,\dots,M \tag{4.24}$$

where $\{\lambda_n, \psi_n\}$is the eigensystem of the scattering matrix **L** and U_k is the k[th] column of U. Consequently, the final indicator function is computed as:

$$W(z_k) = \sum_l W(z_k, f_l)\,\Delta f_l; \quad k \in 1,2,\dots,M \tag{4.25}$$

where $\{\Delta f_l\}$ is the Jacobian resulting from the integration in (4.21) and $W(z_k, f_l)$ is the indicator function at frequency f_l, which is computed from (4.23) or (4.24).

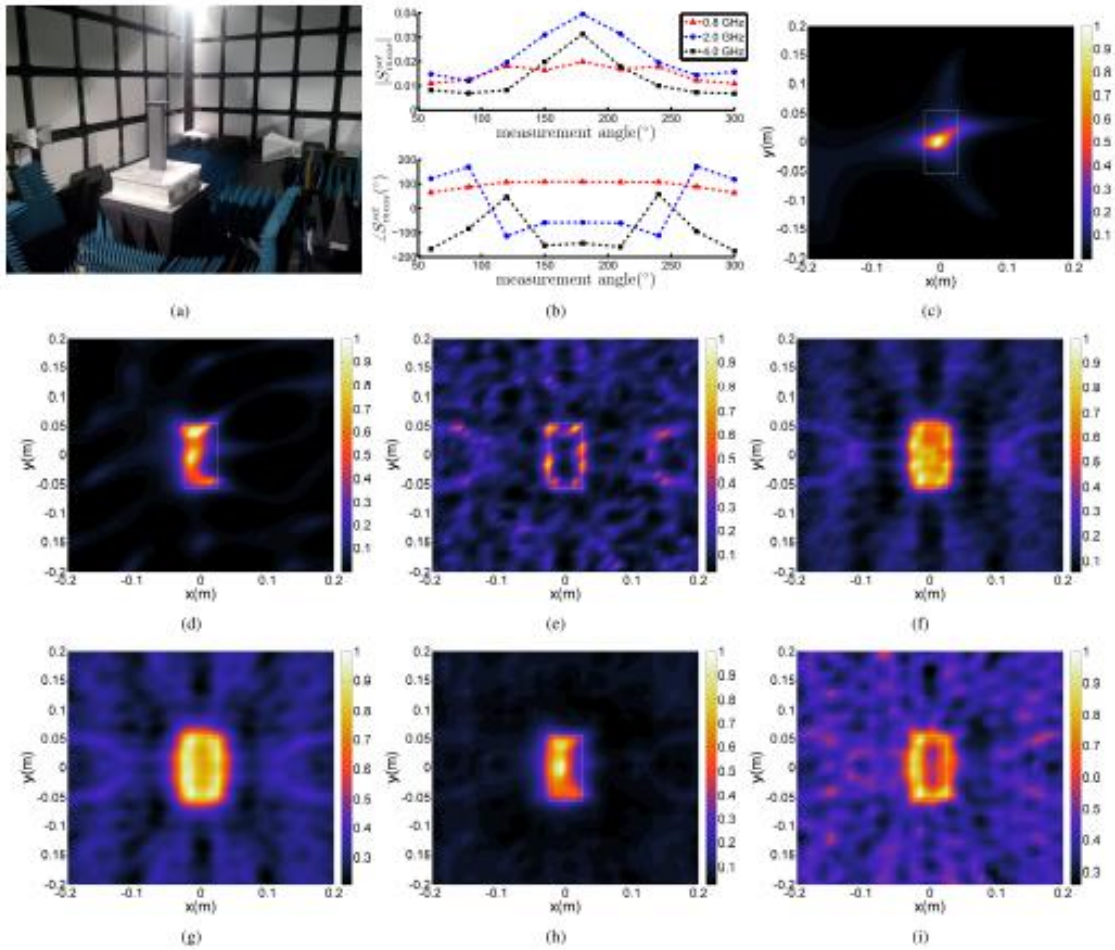

Figure 4.3 : (a) Experimental configuration for single metallic scatterer case. (b) Amplitude and phase of the measured scattered S-parameters of the rectangular target at 0.8, 2.0 and 4.0 GHz. (Transmitting antenna is located at 0°.) Result obtained with: (c) LSM, at 0.8 GHz. (d) LSM, at 2.0 GHz. (e) LSM, at 4.0 GHz. (f) LSM, using all frequencies. (g) FM, using all frequencies. (h) LSM, with calibration in [42], using all frequencies. (i) FM, with calibration in [42], using all frequencies. (Exact borders are marked with dashed white lines.)

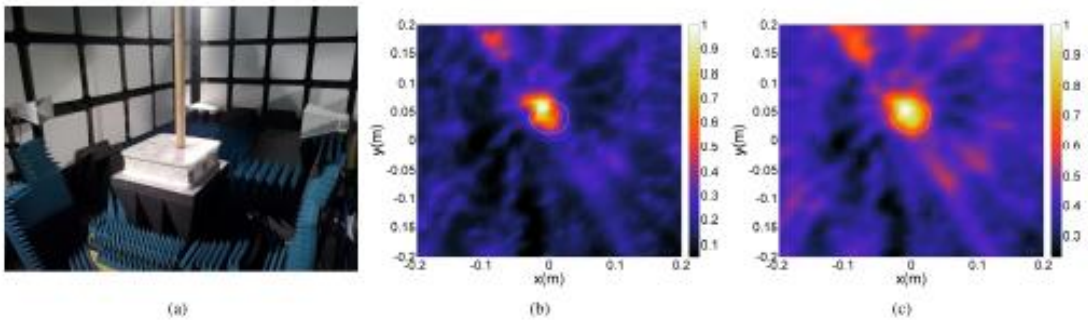

Figure 4.4 : (a) Experimental configuration for single dielectric scatterer case. Result obtained with: (b) LSM, using all frequencies. (c) FM, using all frequencies. (Exact borders are marked with dashed white lines.)

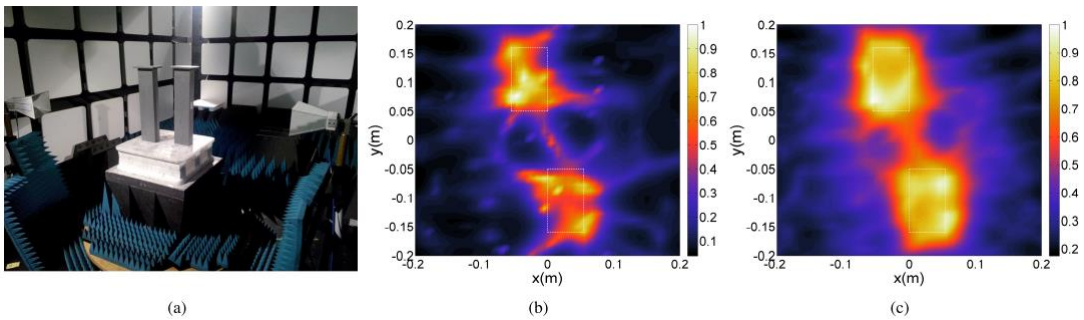

Figure 4.5 : (a) Experimental configuration for multiple metallic scatterers case. Result obtained with: (b) LSM, using all frequencies. (c) FM, using all frequencies. (Exact borders are marked with dashed white lines.)

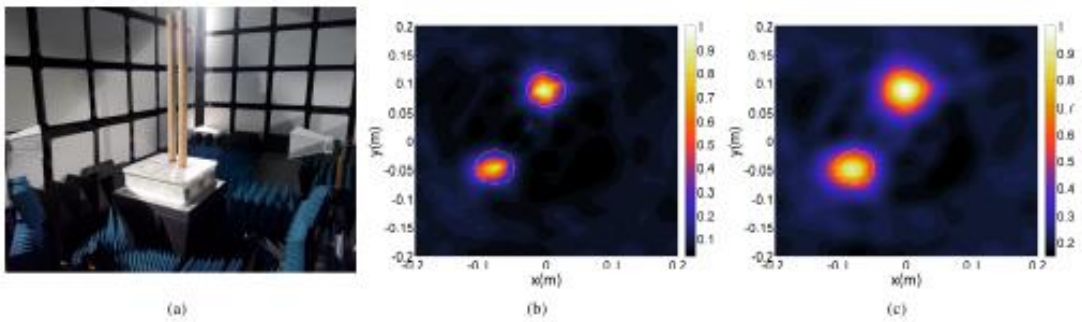

Figure 4.6 : (a) Experimental configuration for multiple dielectric scatterers case. Result obtained with: (b) LSM, using all frequencies. (c) FM, using all frequencies. (Exact borders are marked with dashed white lines.)

Table 4.1 : Localization Errors (ϵ_{loc}: Quality Measure in (4.26), T: Threshold)

Name	$\epsilon_{loc}(\%)$	T	Name	$\epsilon_{loc}(\%)$	T	Name	$\epsilon_{loc}(\%)$	T
4.3(c)	3.50	0.7	4.3(h)	2.81	0.7	4.5(c)	5.81	0.7
4.3(d)	3.19	0.7	4.3(i)	2.31	0.7	4.6(b)	2.69	0.7
4.3(e)	3.44	0.7	4.4(b)	1.38	0.7	4.6(c)	1.19	0.7
4.3(f)	1.69	0.7	4.4(c)	1.13	0.7	4.7(b)	1.96	0.5
4.3(g)	0.56	0.7	4.5(b)	5.94	0.7	4.7(c)	3.87	0.5

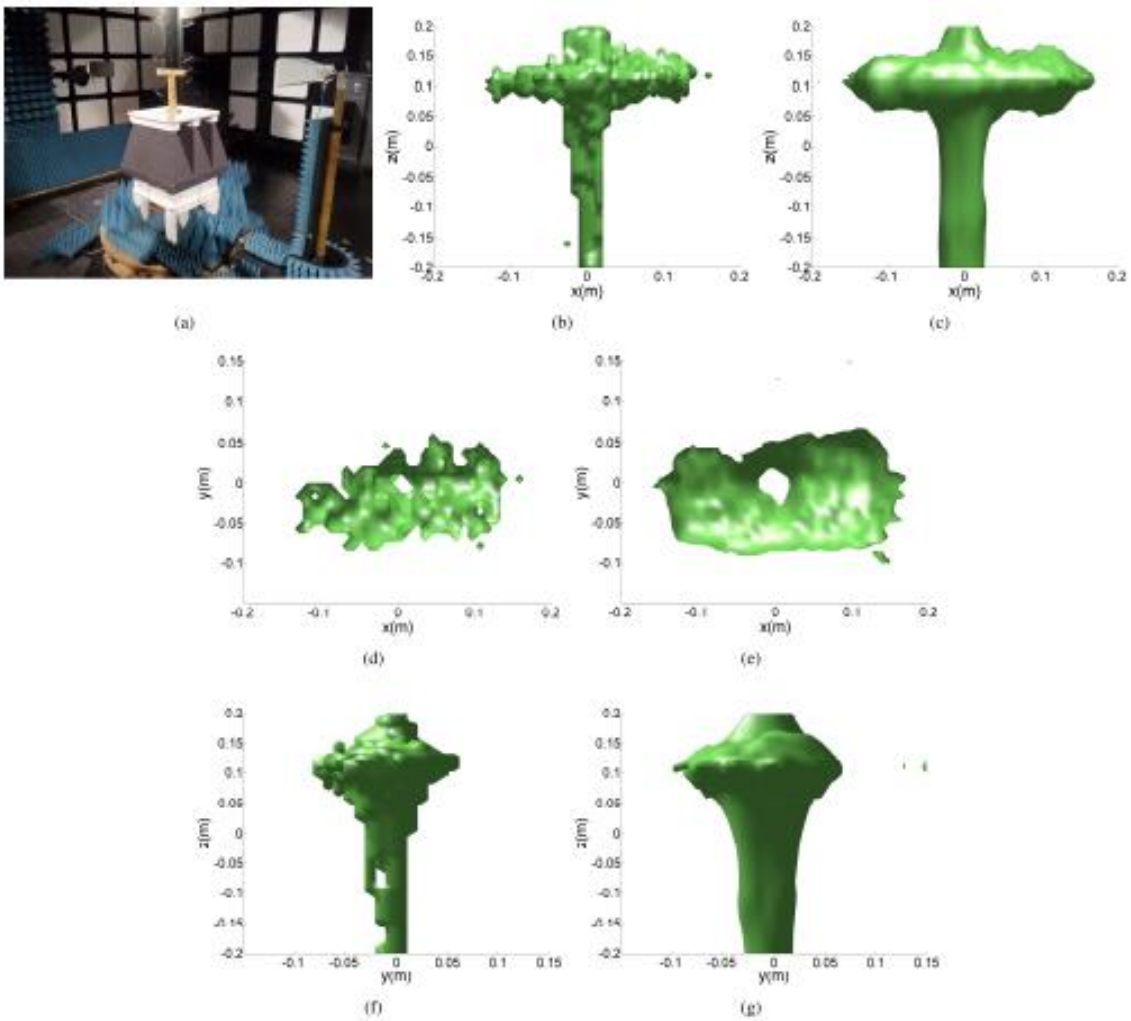

Figure 4.7 : (a) Experimental configuration for T-shaped object. Result obtained with: (b) LSM, xz view, using all frequencies. (c) FM, xz view, using all frequencies. (d) LSM, xy view, using all frequencies. (e) FM, xy view, using all frequencies. (f) LSM, yz view, using all frequencies. (g) FM, yz view, using all frequencies.

4.4 Experimental Verification

Experimental configurations shown through Figure 4.3(a) to Figure 4.7(a) are set up inside an anechoic chamber to verify the developed formulations with measured S-parameters. The measurement system employs a VNA (Agilent N5230A) to measure the S-parameters. For each configuration, the reference frame is chosen as the right handed coordinate system whose z-axis is vertical to the ground plane and whose y-axis is directed towards the antenna on the right side. Unless otherwise stated, measurements are performed on a circle located in the z = 0 m plane with two ridged horn antennas, which are polarized in z direction. For the results given through Figure 4.3 - Figure 4.6 the antennas are positioned at R = 0.85 m away from the center, whereas for the results given in Figure 4.7 they are located on a R = 1 m radius circle. The calibration between the reference plane of the VNA and the input of the antennas is made by using an Agilent N4691B electronic calibration module. We utilize HFSS from Ansys to simulate the realistic antenna models when computing the coefficients in (4.9). The optimal number of harmonics is determined as explained previously. For the above mentioned ridged horn antennas, it is calculated that the harmonics upto order 10 ($1 \leq p \leq 10$) must be used in (4.9) in order to achieve an error norm less than $\tau = 0.01$, which is sufficient for the experiments as it can be observed from Figure 4.2. Note that both LSM and FM require to measure all tangential components of the scattered vector S-parameters on the observation surface Λ. However, measuring only one component of the vector S-parameters is demonstrated to be enough in many cases [14,28,29,42,44,45]. Hence, only the z component of the scattered vector S-parameters is measured for all reconstructions and the collected data is used in (4.19), (4.20) without any pre-processing. The sampling domain D is selected as a square $40 \times 40\ cm^2$ lattice for the reconstructions in Figure 4.3 - Figure 4.6 and a $40 \times 40 \times 30\ cm^3$ prism for the results in Figure 4.7. For all cases, the sampling points are equidistantly distributed with 1 cm separations in each directions and the values of the indicator functions are calculated for the entire lattice. Then, these indicators are normalized with respect to their maximum value to force all images to the same scale. After obtaining the normalized indicator functions $W_n(z_k)$, the qualities of the reconstructions are assessed by the localization error:

$$\epsilon_{loc} = \frac{N_{MP}}{N_{SP}} \tag{4.26}$$

where N_{MP} and N_{SP} are the number of misclassified pixels and sampling points respectively [14,49]. Here a point z_k is classified as a pixel inside a scatterer if $W_n(z_k) \geq T$, where $W_n(z_k)$ is the heuristically selected threshold. [44,49].

As a first experiment to verify the presented formulations, the rectangular metallic object shown in Figure 4.3(a) is measured. Dimensions of this object are 5 cm×11 cm×50 cm and measurements are taken at 11 different frequencies, which are uniformly distributed between 800 MHz and 4.8 GHz. The object is positioned at the center and S-parameters are sampled with 30° angular variations, thus in total 12×12 measurements are performed for each frequency. In Figure 4.3(b), measured S-parameters are plotted for the incidence angle of 0° degrees. Reconstructed images of the rectangular scatterer with LSM are given in Figure 4.3(c), Figure 4.3(d) and Figure 4.3(e), for 0.8 GHz, 2.0 GHz and 4.0 GHz, respectively. From these results one can infer that using single frequency data individually can produce blurry reconstructions, as in Figure 4.3(c), even if the number of measurements is sufficient [62]. The reconstructions for the multi-frequency case are given in Figure 4.3(f) for LSM and Figure 4.3(g) for FM. As it can be observed from these results and the values of ϵ_{loc} given in Table I, using multi-frequency data mitigates the effect of the noise and reconstructions become more accurate.

For the sake of completeness, here we proceed with a comparison of the presented formulations against their electric field counterparts. As mentioned earlier, the electric field based formulations require scattered electric field, which can be obtained with standard calibration procedures. Such calibration methods are based on calculating coefficients γ by comparing simulated electric field and measured S-parameters of a canonical target. After the coefficients are computed, the scattered electric field of any target $E^{sct}(f,x,y)$ is assumed as:

$$E^{sct}(f,x,y) = \gamma(f,x,y)S^{sct}(f,x,y) \tag{4.27}$$

Here the coefficient γ is generally dependent on the illumination frequency f, the position of transmitter x, and the position of receiver y. In this paper the calibration procedure in [42], where the coefficients γ are assumed to be only a function of the illumination frequency f, is used to obtain the scattered electric field. The explicit formula for γ is given as [42]:

$$\gamma(f) = \frac{\sum_x \sum_y E^{sim,ref}(f,x,y)\left(S^{meas,ref}\right)^*(f,x,y)}{\sum_x \sum_y |S^{meas,ref}(f,x,y)|^2} \tag{4.28}$$

where $(\cdot)^*$ denotes complex conjugation and $E^{sim,ref}$, $S^{meas,ref}$ stand for the simulated scattered electric fields, the measured scattered S-parameters for the reference target. As the canonical target, a metallic sphere with radius of 5 cm is employed and its measured S-parameters are compared with the analytical solution [63]. The imaging results for the electric field based inversions are given in Figure 4.3(h) for LSM and Figure 4.3(i) for FM. The localization errors indicate that the presented formulations perform slightly better than the electric field based methods, but as it can be seen from Figure 4.3(f) - Figure 4.3(i), both procedures can accurately determine the shape and position of the object. One of the reason for this small performance difference can be the inclusion of the antenna radiation characteristics into the presented formulations. Consequently, these results can only give an idea about the performance of the S-parameter based formulations compared to their electric field based counterparts. For a comparison of the existing calibration techniques we propose the reader to see [64].

From the aspect of computational complexity, the requirements of the presented formulations are very close to the original LSM and FM formulations, since the mathematical operations are the same except for the computation of the incident field. The calculation of each term in (4.9) takes approximately the same time as the computation of the electric Green's function, which may cause S-parameter based inversions to be slower than their electric field complements. The time difference is not significant for the multi-frequency reconstructions presented in Figure 4.3, where generation of each result takes less than 1 minute on a standard PC. As the number of sampling points increases the total duration becomes noticeable, particularly, the results in Figure 4.7 take 15 minutes on the same PC. Nevertheless, the computation time solely depends on the order of expansion in (4.9), which changes from antenna to antenna. On the other hand, if we consider the calculation of antenna coefficients α, β and the calibration coefficients γ in (4.27), both require a single simulation for each illumination frequency. However, the calibration coefficients γ are unique to the experimental setup whereas antenna coefficients α, β are reusable as long as the electrical properties of the surrounding medium remain the same.

Next, to verify the presented formulations for dielectric structures, the same measurements are repeated for a wooden cylinder with diameter 5.9 cm and height 100 cm as shown in Figure 4.4(a). The object is intentionally placed off-centered and reconstructed images of the cross-section are shown in Figure 4.4(b) and Figure 4.4(c), for LSM and FM respectively. The methods successfully reconstruct dielectric targets as well and obtained images are quite comparable with each other, as can be understood from Table I. These results not only verify the presented formulations but also demonstrate flexibility of qualitative inverse scattering methods, since LSM and FM can be applied to both dielectric and conducting objects without any modification. Furthermore, the localization errors given in Table I indicate that the quality of reconstructions for both kinds of scatterers is quite similar. Indeed, this is an expected outcome, since the number of measurements is sufficient for solving the inverse imaging problem [62]. Another reason for this phenomenon can be the resistance of these algorithms against the marginal variations in the multiple scattering (or nonlinearity) [65].

As mentioned earlier, one of the advantages of qualitative inverse scattering methods is that these methods do not require the number of scatterers a-priori. To demonstrate this capability, the measurement configuration shown in Figure 4.5(a) is prepared. In this case, two rectangular metallic objects having dimensions of 5 cm×11 cm×50 cm are placed off-centered. S-parameter measurements are performed in 1 – 3 GHz range with 250 MHz steps and antennas are rotated with 15° angular variations. Thereby, in total 24×24 measurements are performed for each illumination frequency. Using multi-frequency data with LSM and FM, the results given in Figure 4.5(b) and Figure 4.5(c) are obtained respectively. While the result in Figure 4.5(c) reveals the shape of scatterers more clearly, the error norms in Table I imply that the reconstructions of LSM and FM have almost the same quality for this particular setup.

To further investigate performance of the formulations with multiple dielectric scatterers, another measurement configuration is prepared as shown in Figure 4.6(a). In this setup, two identical wooden cylinders with diameters 5.9 cm and heights 100 cm are placed off-centered. The same measurements, which are performed for multiple metallic scatterers, are repeated for this configuration. Reconstructed images are shown in Figure 4.6(b) for LSM and Figure 4.6(c) for FM. By examining the error values in Table I, it can be inferred that FM produces more satisfying reconstruction

compared to LSM. Apart from that, in contrast to the single scatterer case, the quality of Figure 4.6(b) and Figure 4.6(c) is relatively higher than the quality of the reconstructions for multiple metallic scatterers case, which are given in Figure 4.5(b) and Figure 4.5(c). This performance degradation can be ascribed to several factors: different errors in the measurement process (the errors due to misplacement of the antennas or the objects, random measurement errors) or the selection of the threshold level T etc. Another reason, which causes this deterioration, could be a slight increase in the multiple scattering effect between the antennas and the targets due to the conductor scatterers [65].

Finally, the increase in the number of degrees of freedom for the conductor targets, which is due to their larger size when compared to dielectrics, can have an impact on the quality of the results [62]. Nonetheless, the results demonstrated through Figure 4.5 - Figure 4.6 indicate that the presented methods can tolerate such effects up to a certain extent. Finally, to illustrate 3D reconstruction capability of the methodologies, another experimental setup shown in Figure 4.7(a) is designed. For this case, the target is selected to be a T-shaped object, which consists of two rectangular prisms of wood having dimensions of 4 cm×4 cm×30 cm. This T-shaped object is placed on a small reference stick for ease of physical stabilization. S-parameters are measured within a frequency range of 1−6 GHz with 250 MHz steps. To be able to reconstruct dimensions along the z-axis, measurements for this configuration are performed with 15° angular variations on five different planes, which are z = 0 cm, z = 5 cm, z = 10 cm, z = 15 cm and z = 20 cm surfaces. Thus, in total 120 × 120 bistatic measurements are performed for this particular case. After obtaining the scattering matrix from these measurements, indicator functions are computed using (4.23), (4.25) and (4.24), (4.25) for LSM and FM, respectively. Finally, to have a reconstruction of the T-shaped object, the indicator function is normalized to its maximum value and the W = 0.5 surface is plotted for both algorithms. Results are given in Figure 4.7(b), Figure 4.7(d), Figure 4.7(f) for LSM and in Figure 4.7(c), Figure 4.7(e), Figure 4.7(g) for FM. From the reconstructions, it is clear that both algorithms correctly reconstruct the shape and dimensions of the investigated object, while the error levels in Table I imply that the result of LSM is slightly better than that of FM. This quality difference is related to the choice of regularization parameter, which is critical for LSM as noted earlier.

These results are quite important to demonstrate 3D imaging capability of developed formulations.

Consequently, achieved reconstructions can be improved in many aspects such as increasing the total number of measurements and applying further image processing techniques to obtained images. However, we have implemented the experiments with a minimalistic approach (with minimum number of measurements and without using any pre- or post- processing) to verify the presented formulations.

4.5 Conclusions and Future Work

In this paper, we have developed S-parameters based novel formulations of two closely related qualitative inverse scattering methods, which are the linear sampling method (LSM) and the factorization method (FM). The proposed algorithms include the antenna radiation pattern implicitly, which makes it possible to work with realistic antennas. Besides, they relieve us from any pre- or post- processing steps in exchange for computation of a finite number of antenna parameters. Beyond this, S-parameter based methods have the same computational complexity as their electric field complements.

Apart from introducing S-parameter based LSM and FM, we have experimentally verified them with real measurements for various configurations. It has been demonstrated that S-parameter based formulations yield high quality reconstructions for multi-frequency measurements.

Finally, it is worth mentioning that the developed framework can provide a guideline to reformulate other qualitative inverse scattering methods in terms of S-parameters. Future research will be devoted to extending the presented model for imaging of targets embedded inside inhomogeneous mediums in order to utilize them in real world problems, such as medical imaging and non-destructive testing.

5. EXPERIMENTAL ASSESSMENT OF LINEAR SAMPLING AND FACTORIZATION METHODS FOR MICROWAVE IMAGING OF CONCEALED TARGETS[3]

Shape reconstruction methods are particularly well suited for imaging of concealed targets. Yet, these methods are rarely employed in real nondestructive testing applications, since they generally require the electrical parameters of outer object as a priori knowledge. In this regard, we propose an approach to relieve two well known shape reconstruction algorithms, which are the linear sampling and the factorization methods, from the requirement of the a priori knowledge on electrical parameters of the surrounding medium. The idea behind this paper is that if a measurement of the reference medium can be supplied to these methods, reconstructions with very high qualities can be obtained even when there is no information about the electrical parameters of the surrounding medium. Taking the advantage of this idea, we consider that it is possible to use shape reconstruction methods in buried object detection. Accuracy and stability of the obtained results show that both methods can be quite useful for various buried obstacle imaging problems.

5.1 Introduction

Imaging of concealed targets have different applications ranging from medical imaging [66–68] to subsurface sensing [14,19,31,40,50,69]. Main challenge for such problems is that the solution procedures are expected to capture the electrical parameters (relative dielectric constant ϵ_r, conductivity σ) of whole medium, which includes the buried objects [1,5,13,30]. Up to date, many quantitative techniques are developed to obtain the electrical parameter distribution of the whole medium [1,11]. However, the quantitative formulations involve a considerable amount of computational burden. Being contradictory to quantitative techniques, qualitative

[3] This chapter is based on the paper "Akıncı, M. N., Çağlayan, T., Özgür, S., Alkaşı, U., Abbak, M., Çayören, M., 2015. Experimental Assessment of Linear Sampling and Factorization Methods for Microwave Imaging of Concealed Targets. *International Journal of Antennas and Propagation*, 1-11."

inversion methods, which aim to recover only the shape of the scatterers, have relatively simple formulations and require lower computational resources [8,13,30]. In contrast to such obvious advantages, qualitative inversion techniques are rarely employed in buried obstacle detection, since these methods have strong a priori knowledge requirements in their original form. In particular, to be able to detect the shape of an inclusion by means of these methods, we must supply these two a priori pieces of information: (i) the dielectric parameters of the surrounding medium and (ii) the scattered field when there is no buried object inside the surrounding medium [8,13]. It is obvious that fulfilling such strong conditions altogether is of a serious issue in any imaging problem.

There are already several studies to remedy the a priori information problems of qualitative imaging methods [6,7,31–34,70,71]. In [31], the reciprocity gap-linear sampling method (RG-LSM) is utilized to relieve LSM from the above mentioned constraints. In [32–34,71], different qualitative methods are assessed in biomedical applications for which a limited a priori information is available. Finally, in [6,7,70] LSM is employed in quantitative imaging processes, which can provide an estimate of the dielectric parameters of the whole target.

This paper introduces a practical solution procedure for two famous qualitative inversion schemes, which are the linear sampling method (LSM) [9] and the factorization method (FM) [10]. To this end, we propose a strategy to overcome the a priori knowledge requirement on the dielectric parameters of the surrounding medium. Explicitly, we state that it is possible to use LSM and FM in practical situations, whenever the condition (ii) is satisfied. It is important to notice that if (i) is satisfied (ii) is already fulfilled, but the converse is not true. Furthermore, the second condition can be satisfied in certain practical applications like mine sweeping [72,73], subsurface sensing [14,19,31,40,50,69] or through-wall imaging [49,74], and so forth. (For the sake of clarity, let us further explain the through-wall example: it is not easy to completely characterize the dielectric parameters of a wall, but we can easily make a measurement on the different parts of this wall and use one of these measurements as reference.) Consequently, after having the second condition in hand, an accurate shape reconstruction of the inclusion can be obtained by just assuming the outer medium as free space. We prove the effectiveness of the proposed methods with real measurements taken inside an anechoic chamber. Obtained results show that it is

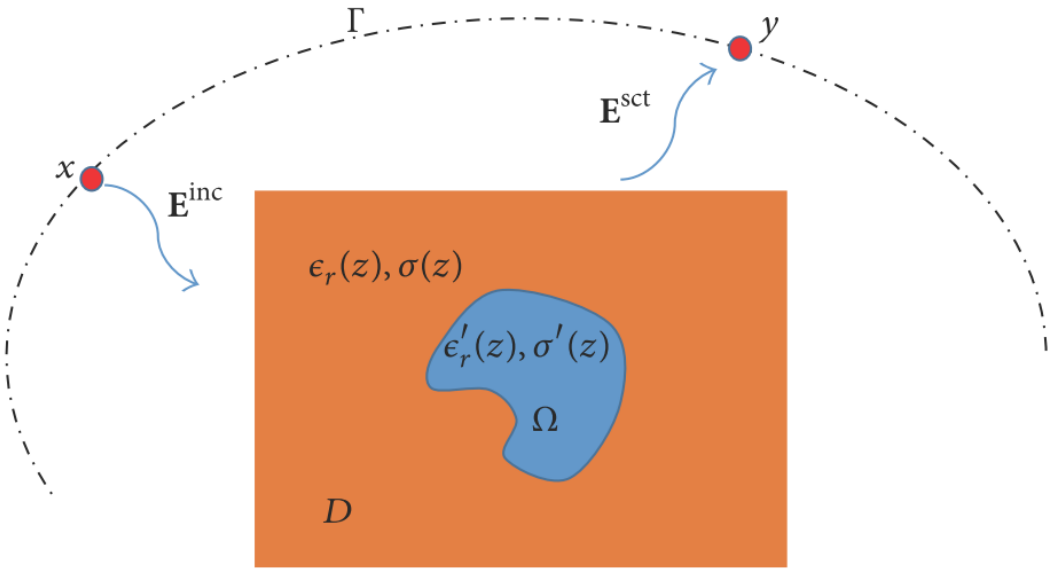

Figure 5.1 : Configuration of the problem (D: the background medium, Ω: the scatterer(s), Γ: the excitation-measurement line, x: the position of the transmitting antenna, y: the position of the receiving antenna, and z: the points inside the sampling domain).

possible to localize the buried obstacles whenever we can find a reference medium, which is available to measurement. In the following section, we briefly revise the LSM and FM, and then, in the subsequent part, we give the formulations of the modified LSM and FM for concealed target detection. Consequently, in the experimental verification section, we will present the results for two different inclusions buried inside dry soil. Throughout the paper, time convention is assumed $exp(-i\omega t)$ and factored out.

5.2 Review of Shape Reconstruction Methods

Consider the scenario in Figure 5.1, where an object Ω, whose relative dielectric permittivity and conductivity are $\epsilon_r'(z)$ and $\sigma'(z)$, is buried into another medium D with electrical parameters of $\epsilon_r(z)$, $\sigma(z)$. The remaining part of the medium is filled with air, which can be modeled as free space. Throughout the paper the wavenumber of any medium is defined as $k = \sqrt{\omega^2\mu\epsilon + i\omega\sigma\mu}$, where ω is the angular frequency of illuminating sources and ϵ, μ are the electrical permittivity, the magnetic permeability of the related medium, respectively. The transmitting and measuring antennas are placed on an arc Γ and we assume that $\Gamma \cap D = \emptyset$; that is, the measurements are done from outside of the surrounding medium. Here, the

measurement arc Γ does not necessarily enclose the object D. The forward scattering mechanism in such a system can be expressed with the well known data and object equations [2]:

$$\mathbf{E^{sct}}(y) = \int_D \mathbf{G}(y,z)O(z)\mathbf{E^{tot}}(z)dz\,;\;\; y \in \Gamma, z \in D \tag{5.1}$$

$$\mathbf{E^{tot}}(z) = \mathbf{E^{inc}}(z) + \int_D \mathbf{G}(z,z')O(z')\mathbf{E^{tot}}(z')dz'\,;\;\; z', z \in D \tag{5.2}$$

where $O(z) = k(z)^2 - k_0^2$ is the so-called object function and $\mathbf{E^{inc}}$, $\mathbf{E^{tot}}$, and $\mathbf{E^{sct}}$ stand for the incident, total, and scattered electric fields, respectively. In (5.1) and (5.2), $\mathbf{G}(\cdot,\cdot)$ is the dyadic Green's function of free space, which is defined as [2]:

$$\mathbf{G}(z,z') = \left(\mathbf{I} + \frac{1}{k_0^2}\nabla\nabla\right)\frac{\exp(ik_0|z-z'|)}{4\pi|z-z\prime|} \tag{5.3}$$

where **I** denotes the identity tensor.

5.2.1 Linear sampling method

The general objective of the shape reconstruction methods is to recover an estimate of the support of the inclusion Ω, given the electrical properties of background medium D. Using the electrical properties of the background medium D, the scattered field when there is no object in the reference medium $\mathbf{E}_{ref}^{sct}$ can be calculated. Then, the scattered field when there is a scatterer Ω in the reference medium $\mathbf{E}_{all}^{sct}$ is measured. Let us assume that Γ is a circle and all antennas are polarized vertically. Then, it is obvious that only vertical component of the scattered electric field $E_{all}^{v,sct}$ can be measured. To identify the location of the inclusion, such methods use a common mechanism, which is assigning an indicator function to each sampling point in D [8,13]. This indicator function exhibits a particular characteristic when the sampling point belongs to inclusion Ω [8,13]. By plotting the indicator function over all sampling domain D and searching for the locations at which the particular behavior exists one can reconstruct the shape of the inclusion Ω [8,13].

Linear sampling method (LSM) is a common example of such support identification methods [9,44,45,75]. The main problem that LSM aims to solve is the far field equation [9]. In the above mentioned circular measurement configuration, where N vertical polarized antennas are uniformly distributed on a circle having radius R, the discretized far field equation reduces to:

$$\mathbf{Fg} = \widetilde{\mathbf{G}} \tag{5.4}$$

where $\mathbf{g} = [g(x_n, z_q)];\ 1 \le n \le N, 1 \le q \le Q$ is the matrix of coefficients that is to be solved, $\mathbf{F} = [E^{v,sct}(y_m, x_n)] = [E^{v,sct}_{all}(y_m, x_n)] - [E^{v,sct}_{ref}(y_m, x_n)];\ 1 \le m, n \le N$ stands for the discretized far field operator, whose elements are the vertical component of the scattered electric field measured by m^{th} antenna when n^{th} antenna acts as source. In (5.4), $\widetilde{\mathbf{G}} = [\tilde{G}^{vv}(y_m, z_q)];\ 1 \le m \le N, 1 \le q \le Q$ is the vertical component of the electrical field measured at point $z_q \in D, 1 \le q \le Q$ when a vertically polarized infinite small dipole, which is located at the position of m^{th} receiving antenna, illuminates the reference medium. LSM states that the solutions of (5.4) is finite only if the sampling point $z_q \in D, 1 \le q \le Q$ coincides with a scatterer Ω. It is important to note that (5.4) is severely ill posed and a regularization scheme must be utilized to obtain a stable solution [9]. Here, we can utilize from the Tikhonov regularization

$$\mathbf{g} = (\alpha \mathbf{I} + \mathbf{F}^{*}\mathbf{F})^{-1}\mathbf{F}^{*}\widetilde{\mathbf{G}} \tag{5.5}$$

where $(\cdot)^{*}$ stands for the conjugate transpose operator. Here, the regularization parameter α is determined by imposing the following condition:

$$\frac{\sigma_N}{\alpha^2+\sigma_N^2}\frac{\sum_{q=1}^{Q}|\langle \tilde{G}^{vv}(\cdot,z_q),u_N(\cdot)\rangle|}{Q} = \frac{1}{\sigma_1}\max_{1\le q\le Q}|\langle \tilde{G}^{vv}(\cdot,z_q),u_1(\cdot)\rangle| \tag{5.6}$$

where $\langle\cdot,\cdot\rangle$ denotes the inner product on receiving points and $\Sigma = \{\sigma_1, \sigma_2, \ldots, \sigma_N\};\ U = \{u_1, u_2, \ldots, u_N\}$ stand for the singular values, the left singular vectors of **F**, respectively [28]. Hence, the indicator function for LSM is defined as the reciprocal of norm of the solutions of (5.4) [9], which can be given as:

$$I(z_q) := \left(\sum_{n=1}^{N}\left|g(x_n, z_q)\right|^2\right)^{-1}; \quad 1 \le q \le Q \tag{5.7}$$

By plotting *I* on the entire sampling domain, an illustration of the shape of the inclusion Ω can be recovered. For a more detailed investigation of the theoretical framework of the LSM, the reader is proposed to see [9,44].

5.2.2 Factorization method

Another famous support identification algorithm is the factorization method (FM), which is developed as an alternative to LSM [10,11,53]. The purpose of FM is to investigate the solvability of the following matrix equation [10]:

$$(\mathbf{F}^{*}\mathbf{F})^{\frac{1}{4}}\,\mathbf{g} = \widetilde{\mathbf{G}} \tag{5.8}$$

where $\mathbf{F}$ and $\widetilde{\mathbf{G}}$ stand for the far field operator and the matrix of Green's functions defined in (5.4). The equation in (5.8) has finite solutions if and only if the sampling point $z_q \in D, 1 \leq q \leq Q$ coincides with an object Ω [10]. In [10], it is shown that the above equation has finite solutions if and only if:

$$I(z_q) := \left(\sum_{m=1}^{M} \frac{|\langle \tilde{G}^{vv}(\cdot, z_q), \psi_m(\cdot)\rangle^2|}{|\lambda_m|}\right)^{-1}; \quad 1 \leq q \leq Q, M \leq N \tag{5.9}$$

is greater than 0. Here, $\Psi = \{\psi_1, \psi_2, \ldots, \psi_N\}$ and $\Lambda = \{\lambda_1, \lambda_2, \ldots, \lambda_N\}$ are the sets of eigenfunctions-eigenvalues of the far field operator $\mathbf{F}$, respectively. Note that the regularization for (5.9) can be done by a spectral cut-off of the eigensystem of $\mathbf{F}$ at $m = M \leq N$. Similar to the LSM, a plot of I on the sampling domain D gives an estimate of the support of the inclusion. More detailed mathematical discussions regarding FM can be found in [10,11,53].

5.3 Solution to Imaging of Buried Objects

Although the above procedures are simple to implement and stable in nature, they are rarely employed in experimental concealed target detection. This is basically due to the fact that they require some a priori information, which cannot be available in most of the practical problems. Those requirements in the above scenarios can be stated as follows.

(i) Far field equation in (5.4) requires one to know the dyadic Green's function $\widetilde{\mathbf{G}}$, which is directly connected with the electrical parameters of the surround ing medium (i.e., $\epsilon_r(z), \sigma(z)$ in Figure 5.1).

(ii) Furthermore, to be able to construct the equation system in (5.4) the scattered field due to inclusion, that is, $E^{v,sct}$ in (5.4), must be known. Therefore, we must compute (or at least approximate) $E^{v,sct}_{ref}$, which is the scattered field from the reference medium D.

It is very important to distinguish between these two conditions. First of all, satisfying the first condition, which states that one must have dyadic Green's function $\widetilde{\mathbf{G}}$, seems to be unrealistic in many microwave measurement systems. However, the second condition can be satisfied in certain imaging problems for which an extra measurement

of a reference medium is feasible [14,19,31,40,49,50,69,72-74]. As an example, in through-wall imaging or subsurface sensing problems, it is not hard to find a reference medium available to measurement, but measuring such a reference does not provide us a model for the distribution of the electrical parameters of the surrounding medium D. Let us think of such cases in which we have a reference medium available to measurement, and then we propose that the far field equation in (5.4) can be modified as:

$$\mathbf{Fg} = \mathbf{G} \tag{5.10}$$

where Green's function of free space $\mathbf{G}$ is replaced with Green's function of the background medium $\widetilde{\mathbf{G}}$. The dyadic Green's operator $\mathbf{G}$ can be computed by (5.3); therefore, by solving the modified equation in (5.10) via Tikhonov regularization defined in (5.5), (5.6) and by plotting the indicator function I as in (5.7), an estimate of the support of the inclusion Ω can be obtained.

Similarly, the main equation of FM can be changed as:

$$(\mathbf{F}^{*}\mathbf{F})^{\frac{1}{4}}\,\mathbf{g} = \mathbf{G} \tag{5.11}$$

Hence, the indicator function I for FM can be obtained in a similar manner to (5.9). Although there are different approaches for an optimal regularization of the FM [76,77], we set $M = N$ by relying on our numerical observations. Consequently, a plot of I over the entire sampling domain D provides a reconstruction of the shape of the buried targets.

5.4 Experimental Verification

In the light of the theoretical evaluations, this section includes the discussions of what kind of results can be obtained for different scatterers and for what applications the approach that we have proposed can be useful. To illustrate the applicability of the methodologies, we prepare the measurement setup shown in Figure 5.2. The system consists of computer controlled turn table, a vector network analyzer (VNA, Agilent N5230A), and two vertically polarized Vivaldi

Figure 5.2 : Measurement setup.

antennas, which are examples of classical ultrawideband antennas [61,78-80]. Calibration between VNA and the antennas is done by means of the Agilent N4691B electronic calibration module. For all cases, the reference medium is dry soil. S-parameters are sampled at 24 points when the scatterer is chosen as water and 12 points when the scatterer is air. (The number of measurements is selected according to the number of degrees of freedom of the scattering problem. Note that the radii of the targets are smaller than one wavelength (wavelength in free-space) even for the highest frequency. Hence $2k_0a \approx 12$ measurements are sufficient in general. To guarantee a better reconstruction quality for the water filled target, we increase the number of measurements to 24 [62].) Unless otherwise stated, the measurement points are uniformly distributed on the circle having a radius of 17 cm. For the conversion between S-parameters and electric field, the method proposed in [42] is employed. Basically, using a canonical target, a single coefficient for each frequency f, is calculated as:

$$C(f) := \frac{\sum_x \sum_y E_{sim}(x,y,f) S^*_{meas}(x,y,f)}{\sum_x \sum_y |S_{meas}(x,y,f)|^2}; \qquad (5.12)$$

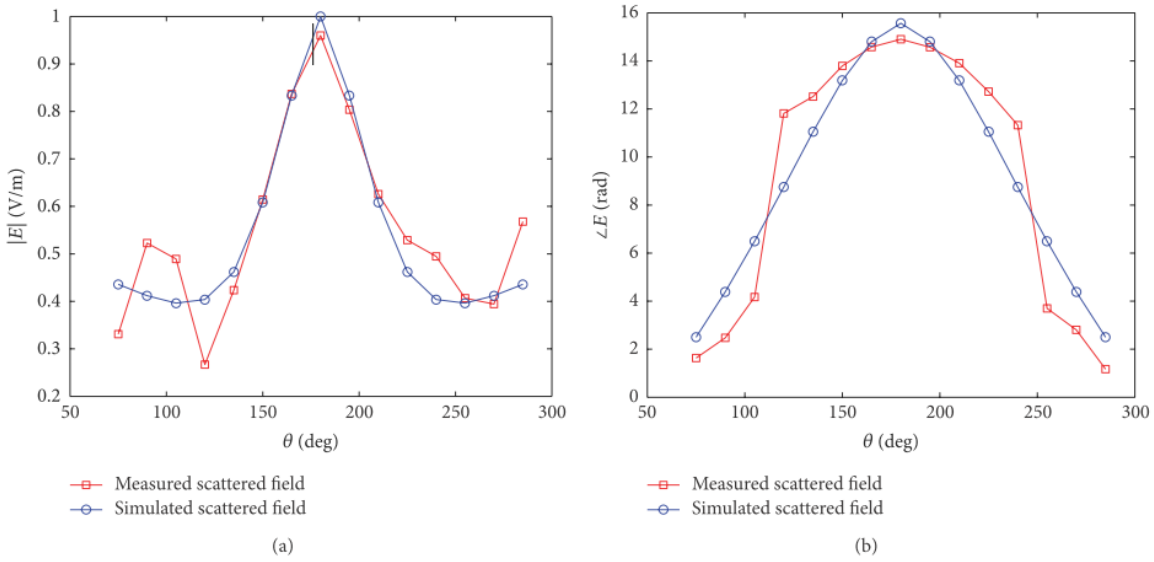

Figure 5.3 : Measured (red squares) and simulated (blue circles) electric fields for canonical target at 4 GHz: (a) normalized absolute values (b) phase.

where $E_{sim}(x, y)$ denotes the vertical component of simulated scattered field and $S_{meas}(x, y)$ stands for the measured scattered S-parameter for the same polarization.

In (5.12), the transmitter is located at x, whereas the position of the receiver is given by y. After calculating the conversion coefficients (f), the vertical component of the scattered electrical field for any target can be given as:

$$E_{meas}(x, y, f) = C(f)S_{meas}(x, y, f) \tag{5.13}$$

In our measurement configuration, the calibration target is selected as a metallic cylinder with a radius of 10 cm and its simulated field is computed analytically [63]. As given in Figure 5.3, calibrated electric field of the cylinder and the analytical solution have a good agreement. To increase the frequency diversity of the measurement, S-parameters are sampled at 41 frequencies equilinearly distributed on 2 GHz–6 GHz interval. Multifrequency reconstructions are obtained by summing all single frequency indicators and normalizing the final values with respect to their maximum value [55]. To be able to make pointwise summations on single frequency reconstructions, the sampling domain is discretized into 40×40 points for all frequencies. As a final note, it must be emphasized that this measurement setup can only produce 2D slice images, since the antennas do not sweep along vertical axis [28]. Therefore, all reconstructions given here is for the horizontal slice going through the midpoints of the

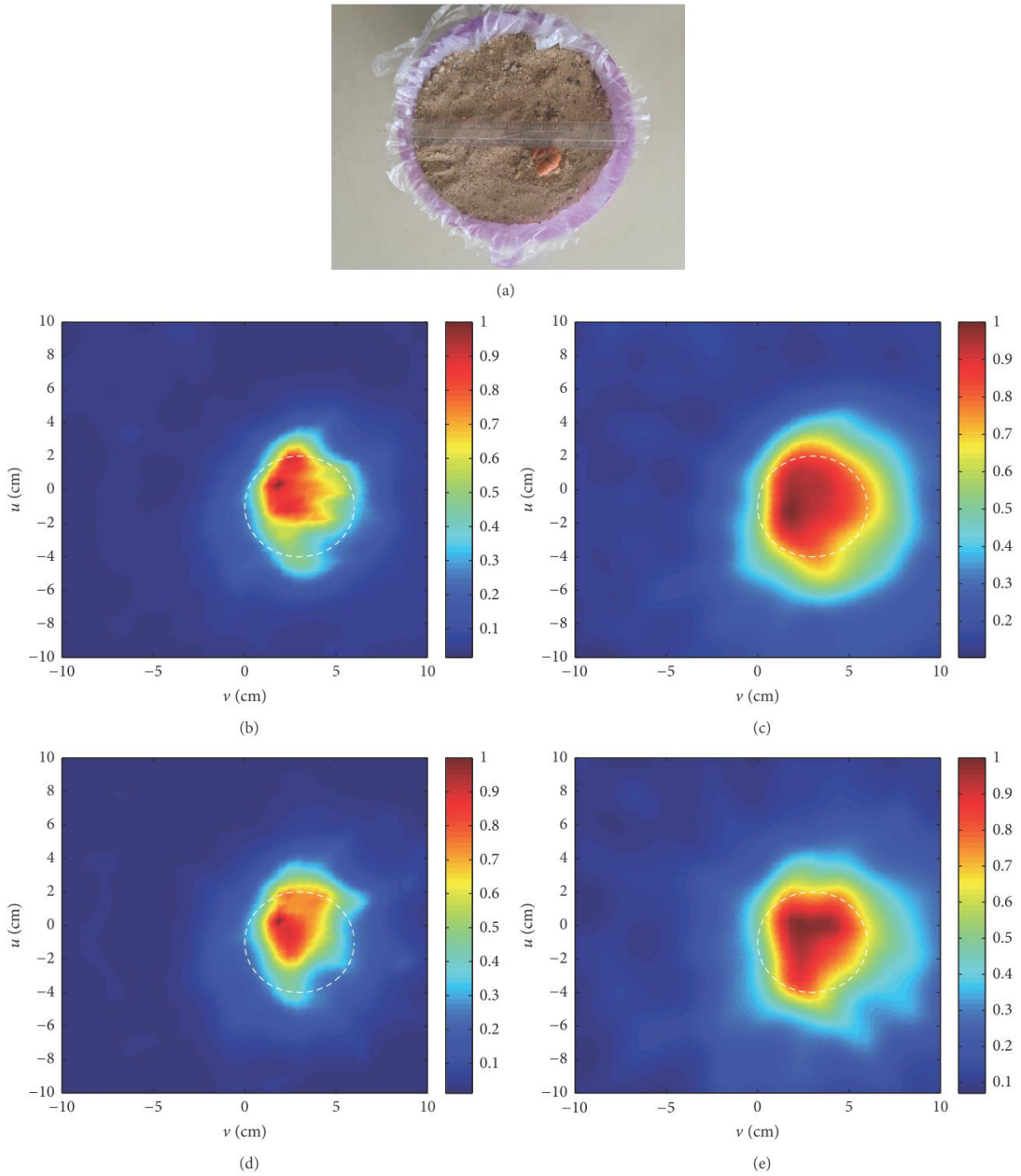

Figure 5.4 : (a) Measured material, (b) LSM reconstruction with the proposed formulation, (c) FM reconstruction with the proposed formulation, (d) LSM reconstruction with the exact Green's function, and (e) FM reconstruction with the exact Green's function, for the scatterer filled with water.

antennas. (Although we stress that the algorithms produce 2D images, full 3D modeling is employed for all configurations. Explicitly, the equations given in (5.10), (5.11) are solved without simplifying the operators to 2D case. The only modification is that (5.10) and (5.11) are solved for only those points, which belong to the horizontal slice that is going through the midpoints of the antennas.)

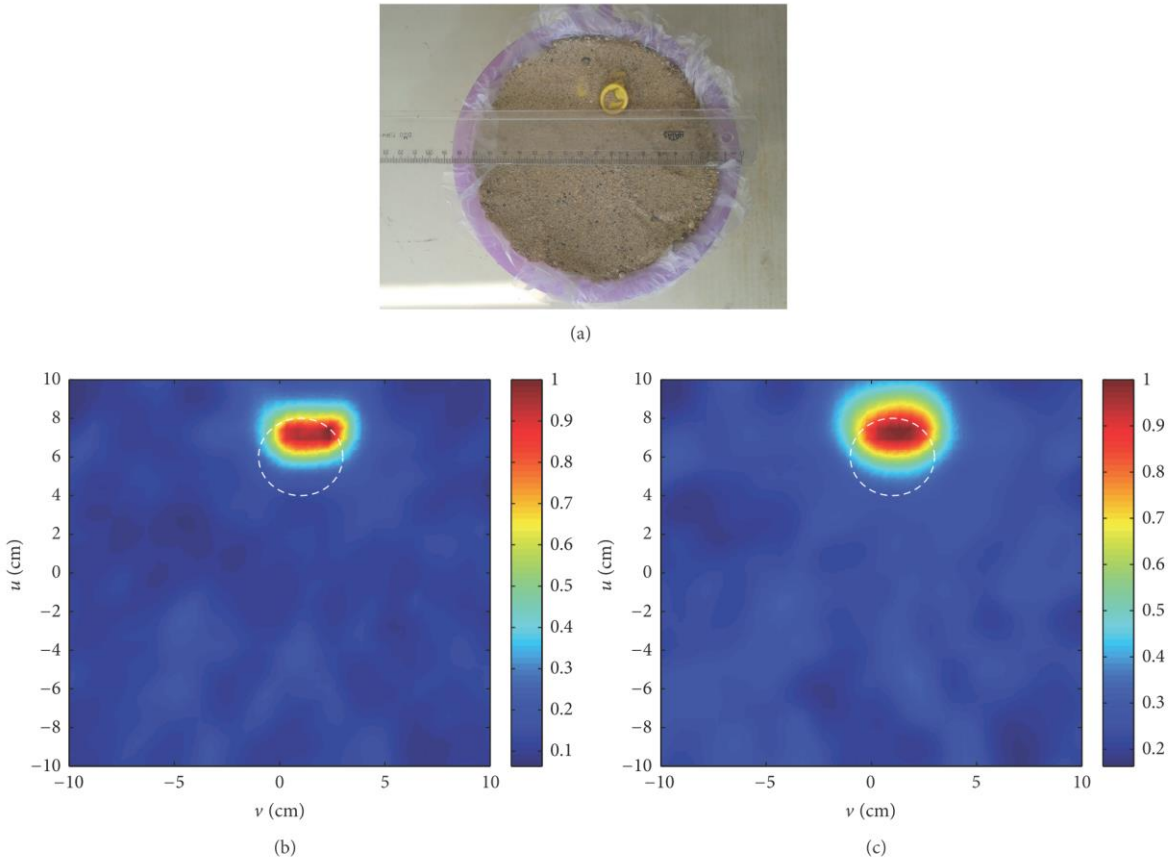

Figure 5.5 : (a) Measured material, (b) LSM reconstruction, and (c) FM reconstruction for the scatterer filled with air.

The first material, for which the measurements are performed, is shown in Figure 5.4(a). In this case, two measurements are performed. First the dry soil is measured and, then for the second measurement, a water filled balloon with a radius of 3 cm is buried into soil. The center of the balloon is located at (u =− 1 cm, v = 3 cm). Here, we adopt the following axis definitions: v axis is parallel to ruler in Figures 5.4(a) and 5.5(a) and its positive end is directed towards right side, u is the axis, which can be obtained by rotating v at an amount of 90° in the counter clockwise direction. Obtained results for LSM and FM are given in Figures 5.4(b) and 5.4(c), respectively. Obviously, both methods recover the horizontal profile correctly without using any a priori knowledge on the electrical properties of the dry soil. An important point that must be mentioned is that both algorithms reconstruct the support of the midslice of the inclusion, although the antennas are not aligned with the midslice of the scatterer. By referring to our empirical observations, we can say that these methods exhibit this peculiar behavior in general. Another interesting point is the quality of the reconstructions for these two methods are very close to each other.

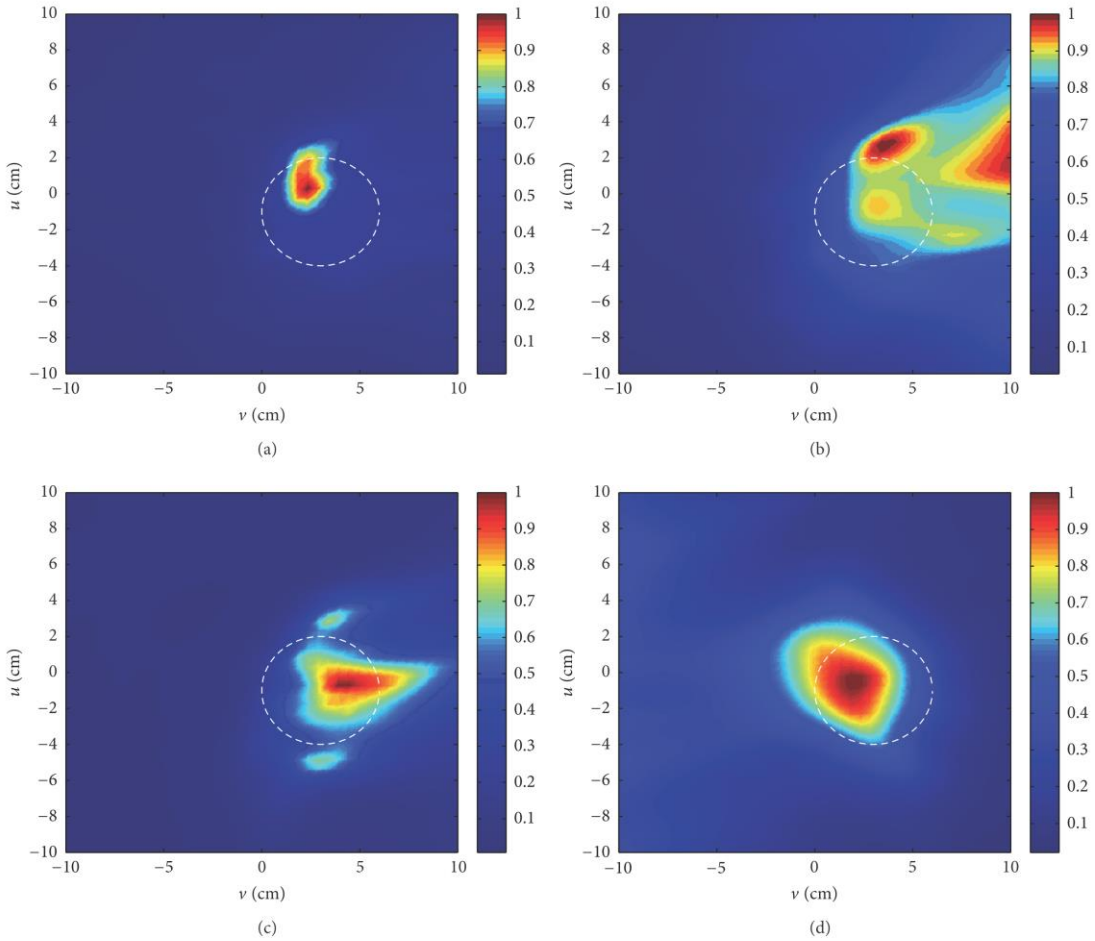

Figure 5.6 : Reconstructions obtained for the water filled scatterer by using (a) LSM, (b) FM when the transmitting and receiving antennas are located on $90° < \theta < 270°$, $r =$ 17 cm, and (c) LSM, (d) FM when the transmitting and receiving antennas are located on $90° < \theta < 270°$, $r =$ 17 cm, and $-90° < \theta < 90°$, $r =$ 17 cm, respectively. (Here $\theta = \tan^{-1}(\frac{u}{v})$ and $r = \sqrt{u^2 + v^2}$.)

This in fact is expected since these methods originate from similar mathematical principles.

After demonstrating the applicability of the proposed approach, we investigate how the information of the exact Green's function affects the quality of the results. For this aim, the dyadic Green's function of the reference medium is computed with a 3D Method of Moments solver, utilized from biconjugate gradient fast Fourier transform method [35]. Here, the relative dielectric permittivity and conductivity of the dry soil is taken as $\epsilon_r =$ 3.5 and $\sigma =$ 0.05 $\frac{S}{m}$ for all frequencies of illumination [81,82]. The results with the exact Green's function are given in Figures 5.4(d) and 5.4(e) for LSM and FM, respectively. As can be seen the reconstructions of proposed formulations

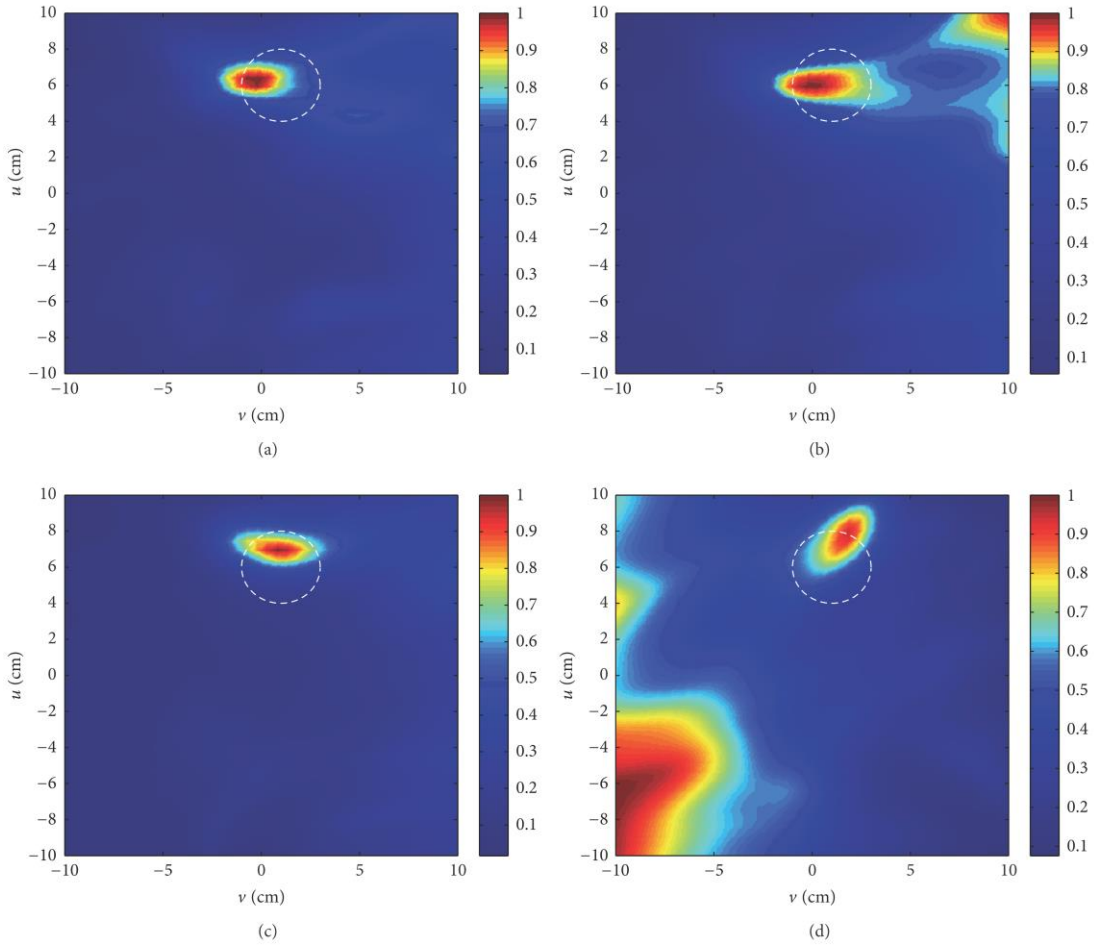

Figure 5.7 : Reconstructions obtained for the air-filled scatterer by using (a) LSM, (b) FM when the transmitting and receiving antennas are located on $90° < \theta < 270°$. (c) LSM, (d) FM when the transmitting and receiving antennas are located on $90° < \theta < 270°$, $r =$ 17 cm, and $-90° < \theta < 90°$, $r =$ 17 cm, respectively.

are very similar to Figures 5.4(d) and 5.4(e). Hence, it can be concluded that, with the proposed method, unavailability of the exact dyadic Green's function does not cause a significant quality degradation.

Next, we continue with a second example to further illustrate the performance when the scatterer is weak (i.e., the electrical properties of the buried material is low.) and the electrical contrast between the inclusion and the surrounding medium is low. (Note that the electrical properties of the water is ϵr = 75 and σ= 2 S/m at 3 GHz [83].) To this end, the material shown in Figure 5.5(a) is prepared. For this case, an air filled balloon is buried into dry soil. The coordinates of the center of the balloon are measured as (u= 6 cm, v = 1 cm) and the radius of the scatterer is 2 cm. Reconstructions for LSM and FM are shown in Figures 5.5(b) and 5.5(c), respectively.

As it can be observed from the results, the proposed formulations produce an estimate of the shape of the inclusion even when the scatterer is weaker in electrical contrast.

Up to now, we show the feasibility of the presented method when the measurements are taken on a full aperture. However, the common measurement schemes for concealed target detection problems consist of a limited incidence-observation angles. Thus, to be able to give a merit to the presented formulations, they must be analyzed when such a measurement configuration is employed. For this aim, certain parts of the obtained scattering matrix are cut and the inversions are applied by using only these measurements. The imaging results when the scatterer is water filled balloon are given in Figure 5.6. Here, for Figures 5.6(a) and 5.6(b), the transmitting and measuring antennas are located on the same arc, which is defined as $90^\circ < \theta < 270^\circ$, r= 17 cm. Such a measurement scheme is mostly employed in subsurface sensing [14,19,31,40,50,69] and through-wall imaging problems [49,74]. As can be seen from the results, the quality of the reconstructions decreases for both LSM and FM, when compared with the previous results. Nevertheless, both methods can provide some clues about the shape of the scatterers. Another typical measurement configuration is the one in which the transmitting and receiving antennas are located on different arcs. Here, the union of these two arcs can enclose the material under test. Such a configuration may be useful in nondestructive testing problems [84-86]. The results for this type of measurement scenario are given in Figures 5.6(c) and 5.6(d) for LSM, FM, respectively. For these results, the scatterer is the water filled balloon as in Figures 5.6(a) and 5.6(b). As can be observed from these images, this kind of measurement produces better reconstructions than the results in Figures 5.6(a) and 5.6(b). This phenomenon can be simply explained as the increase in the union of the measurement-excitation apertures leads to better results.

Finally, the same measurement configurations can be applied to the air filled scatterer. The obtained results, when the transmitting and receiving antennas are located on the same arc, are given in Figures 5.7(a) and 5.7(b) for LSM, FM, respectively. It is obvious that both algorithms are also capable of providing an estimate of the shape of the air filled scatterer. Another point that must be stressed is that the reconstruction for LSM is more clear than the one for FM. In fact, there can be many factors which can cause such performance differences. A few of them can be stated as selection of regularization parameter for LSM, the number of eigenvalues taken into account for

FM and, and so forth. As for the two last examples for the weak scattering target, the case in which the transmitting and receiving antennas are located on different arcs is considered. The obtained reconstructions for LSM and FM are given in Figures 5.7(c) and 5.7(d), respectively. By observing the results, it can be inferred that both methods can give an estimate of the shape and the location of the scatterer. Similar to the results in Figures 5.7(a) and 5.7(b), LSM gives a more clear estimate compared to the FM. This performance difference can be explained by using the same arguments stressed in the above. Consequently, we can conclude that the modified formulations can be employed in such real measurement scenarios to obtain an estimate of the shape and the location of the buried obstacles.

5.5 Conclusions and Future Work

In this paper, we propose an experimental technique to move around the a priori information requirements of the qualitative methods. The proposed approach works for the situations where an extra measurement for the reference medium is feasible. In particular, we modified the formulations of two well known qualitative methods, the linear sampling method (LSM) and the factorization method (FM). The accuracy of the modified formulations is tested against realistic measurements. Besides showing the accuracy of the presented formulations, the obtained results imply the feasibility of proposed approach, especially for subsurface imaging, where the targets are buried into soil.

Lastly, we want to emphasize that the proposed formulations are important from the aspect that it can make the usage of qualitative methods possible in many real world problems. Future research will be devoted to application of these methods in more realistic environments.

6. CONCLUSIONS AND RECOMMENDATIONS

In this thesis, we investigate the application of qualitative inversion techniques in microwave imaging, which are rarely analyzed from an engineering perspective.

The first part of the thesis present a microwave imaging method for detecting and localizing buried objects under a rough air – soil interface. The formulation depends on factorization method in which the positions of scatterers are qualitatively determined with the norm of a properly defined indicator function. The method can retrieve positions and shapes of multiple objects with a near field limited aperture measurement configuration where the measurements are performed with a short antenna array moving over the soil. In particular, the short array of antennas are slided over the surface step by step and measurements are recorded in a bistatic scattering matrix. Here, due to short length of the array only a small portion of the whole bistatic scattering matrix, which is around the diagonal, can be filled with measurements. The parts of the scattering matrix that is missing is simply filled with zeros. This scattering matrix is then utilized in the factorization method and the indicator functions are computed accordingly. Numerical simulations prove that the presented method can be operated in a real-time-like mode where reconstructed image is updated while measurements are still in progress. Moreover, the method is tested for many realistic scenarios such as the roughness of surface is too high or the electrical parameters of the soil is not exactly known and when the surface soil is wrongly estimated. Results show that the proposed method can handle with such realistic challenges upto a certain point.

In the second part of this thesis, S-parameter-based novel formulations of two closely related qualitative inverse scattering methods, which are the LSM and FM, are presented. Historically, LSM and FM are developed by mathematicians under some infeasible assumptions. Then, these methods are applied in many different inverse problems by assuming the input of the LSM and FM is the scattered electric field measurements. Yet, in the real applications the measurements at microwave ranges are exclusively performed with vector network analyzers (VNA), which can only measure scattering parameters. Besides, previous works assume that the exciting and measuring

antennas are singular sources, which are also practically infeasible to obtain. In this direction, we reformulate the LSM and FM when the input of these algorithms are scattering parameters. Furthermore, the proposed algorithms are extended to include the antenna radiation pattern implicitly, which makes it possible to work with realistic antennas. Consequently, the introduced methods relieve us from any pre- or post-processing steps in exchange for computation of a finite number of antenna parameters. The accuracy and stability of presented methods are experimentally verified with real measurements for various configurations.

In the third and last part of this thesis, we take a look on an experimental technique to move around the a priori information requirements of the qualitative methods in concealed target detection. The main challenges that has to be solved for the usage of qualitative methods in concealed target detection are (i) the computation of Green's function of the medium in the hand or in other words finding an appropriate reference medium (ii) the difference between the measured fields between the background+target and background. In general, the fulfilling the condition in (i) is almost impossible but for many concealed target detection problems (ii) can be satisfied with an additional reference medium measurement. In particular, we modified the formulations of two well known qualitative methods, the linear sampling method (LSM) and the factorization method (FM) so that the scattered field data is the difference between background+target and a reference background while the Green's function of the background medium is replaced with the Green's function of free space, which can be computed analytically. The accuracy of the modified formulations is tested against realistic measurements. Besides showing the accuracy of the presented formulations, the obtained results imply the feasibility of proposed approach.

Consequently, it has to be stated that the developed algorithms are in the MMT (Mikrodalga Meme Tomografi – Microwave Breast Tomography) scanner, which is developed by our group named as ITU-ERG (Istanbul Technical University-Electromagnetic Research Group). This scanner is currently tested in the Medical School of Cerrahpaşa University. Our future work is devoted to develop more robust and efficient algorithms to improve the performance of this scanner.

REFERENCES

[1] **Chew W. C. and Wang Y.** (1990). Reconstruction of two-dimensional permittivity distribution using the distorted born iterative method, *IEEE Transactions on Medical Imaging*, 9(2), 218–225.

[2] **Chew W. C.** IEEE press New York. (1995) *Waves and fields in inhomogeneous media.*

[3] **Van Den Berg P. M. and Kleinman R. E.** (1997). A contrast source inversion method, *Inverse problems,* 13(6), 1607.

[4] **Van Den Berg P. M., Van Broekhoven A., and Abubakar A.** (1999). Extended contrast source inversion, *Inverse Problems*, 15(5), p. 1325.

[5] **Abubakar A. and Van Den Berg P. M.** (2002). The contrast source inversion method for location and shape reconstructions, *Inverse Problems*, 18(2), 495.

[6] **Di Donato L., Bevacqua M. T., Crocco L., and Isernia T.** (2015). Inverse scattering via virtual experiments and contrast source regularization, *IEEE Transactions on Antennas and Propagation*, 63(4), 1669–1677.

[7] **Di Donato L. and Crocco L.** (2015). Model-based quantitative cross-borehole gpr imaging via virtual experiments, *IEEE Transactions on Geoscience and Remote Sensing*, 53(8), 4178– 4185.

[8] **Cakoni F. and Colton D.** Springer (2013) *A Qualitative Approach to Inverse Scattering Theory*.

[9] **Cakoni F., Colton D., and Monk P.** SIAM (2011) *The linear sampling method in inverse electromagnetic scattering*.

[10] **Kirsch A. and Grinberg N.** Oxford University Press (2007*) The Factorization Method for Inverse Problems.*

[11] **Kirsch A.** (2004). The factorization method for maxwell's equations, *Inverse Problems*, 20(6), 117.

[12] **Arens T.** (2004). Why linear sampling works, *Inverse Problems*, 20(1), 163.

[13] **Potthast R.** (2006). A survey on sampling and probe methods for inverse problems, *Inverse Problems*, 22(2), R1.

[14] **Catapano I., Crocco L., and Isernia T.** (2008). Improved sampling methods for shape reconstruction of 3-d buried targets, *IEEE Transactions on Geoscience and Remote Sensing*, 46(10), 3265–3273.

[15] **Zakaria, A., Jeffrey, I., and LoVetri, J.** (2013). Full-vectorial parallel finite-element contrast source inversion method. *Progress In Electromagnetics Research*, 142, 463-483.

[16] **Wang, X. Y., Li, M., & Abubakar, A.** (2015). Acceleration of multiplicative regularized contrast source inversion algorithm using paralleled computing device. In *2015 Asia-Pacific Microwave Conference*, Nanjing, China, Dec. 6-9.

[17] **Bevacqua, M. T., and Scapaticci, R.** (2016). A Compressive Sensing Approach for 3D Breast Cancer Microwave Imaging With Magnetic Nanoparticles as Contrast Agent. *IEEE transactions on medical imaging*, 35(2), 665-673.

[18] **Bevacqua, M. T., Crocco, L., Di Donato, L., & Isernia, T.** (2015). Microwave imaging of nonweak targets via compressive sensing and virtual experiments. *IEEE Antennas and Wireless Propagation Letters*, 14, 1035-1038.

[19] **Catapano, I., Soldovieri, F., and Crocco, L.** (2011). On the feasibility of the linear sampling method for 3D GPR surveys. *Progress In Electromagnetics Research*, *118*, 185-203.

[20] **Gebauer, B., Hanke, M., Kirsch, A., Muniz, W., and Schneider, C.** (2005). A sampling method for detecting buried objects using electromagnetic scattering. *Inverse Problems*, *21*(6), 2035.

[21] **Cakoni, F., Fares M., and Haddar, H.** (2006). Analysis of two linear sampling methods applied to electromagnetic imaging of buried objects. *Inverse Problems*, *22*(3), 845.

[22] **Fischer, C., Herschlein, A., Younis, M., and Wiesbeck, W.** (2007). Detection of antipersonnel mines by using the factorization method on multistatic ground-penetrating radar measurements. *IEEE transactions on geoscience and remote sensing*, *45*(1), 85-92.

[23] **Firoozabadi, R., Miller, E. L., Rappaport, C. M., and Morgenthaler, A. W.** (2007). Subsurface sensing of buried objects under a randomly rough surface using scattered electromagnetic field data. *IEEE Transactions on Geoscience and Remote Sensing*, *45*(1), 104-117.

[24] **Catapano, I., and Crocco, L.** (2009). An imaging method for concealed targets. *IEEE Transactions on Geoscience and Remote sensing*, *47*(5), 1301-1309.

[25] **Altuncu, Y., Akduman, I., and Yapar, A.** (2007). Detecting and locating dielectric objects buried under a rough interface. *IEEE Geoscience and Remote Sensing Letters*, *4*(2), 251-255.

[26] **Cmielewski, O., Tortel, H., Litman, A., and Saillard, M.** (2007). A two-step procedure for characterizing obstacles under a rough surface from bistatic measurements. *IEEE Transactions on Geoscience and Remote Sensing*, *45*(9), 2850-2858.

[27] **Grisel, Y., Mouysset, V., Mazet, P. A., and Raymond, J. P.** (2012). Determining the shape of defects in non-absorbing inhomogeneous media from far-field measurements. *Inverse Problems*, *28*(5), 055003.

[28] **Catapano, I., Crocco, L., D'Urso, M., and Isernia, T.** (2009). 3D microwave imaging via preliminary support reconstruction: Testing on the Fresnel 2008 database. *Inverse Problems*, *25*(2), 024002.

[29] **Eskandari, M. R., Dehmollaian, M., and Safian, R.** (2014). Experimental investigation of factorization method as a qualitative approach for near-field microwave imaging. *IEEE Antennas and Wireless Propagation Letters*, *13*, 289-292.

[30] **Pastorino M.** Wiley (2010) *Microwave Imaging*.

[31] **Ozdemir, O., and Haddar, H.** (2010). Preprocessing the reciprocity gap sampling method in buried-object imaging experiments. *IEEE Geoscience and Remote Sensing Letters*, *7*(4), 756-760.

[32] **Colton, D., and Monk, P.** (1998). A linear sampling method for the detection of leukemia using microwaves. *SIAM Journal on Applied Mathematics*, *58*(3), 926-941.

[33] **Colton, D., and Monk, P.** (1999). A linear sampling method for the detection of leukemia using microwaves II. *SIAM Journal on Applied Mathematics*, *60*(1), 241-255.

[34] **Bozza, G., Brignone, M., and Pastorino, M.** (2010). Application of the no-sampling linear sampling method to breast cancer detection. *IEEE Transactions on Biomedical Engineering*, *57*(10), 2525-2534.

[35] **Gan, H., and Chew, W. C.** (1995). A discrete BCG-FFT algorithm for solving 3D inhomogeneous scatterer problems. *Journal of Electromagnetic Waves and Applications*, *9*(10), 1339-1357.

[36] **Altuncu, Y., Yapar, A., and Akduman, I.** (2006). On the scattering of electromagnetic waves by bodies buried in a half-space with locally rough interface. *IEEE transactions on geoscience and remote sensing*, *44*(6), 1435-1443.

[37] **Bondarenko, O., Kirsch, A., and Liu, X.** (2013). The factorization method for inverse acoustic scattering in a layered medium. *Inverse Problems*, *29*(4), 045010.

[38] **Cakoni, F., and Colton. D. L.** Springer (2006) Qualitative Methods in Inverse Scattering Theory: An Introduction.

[39] **Curtis, J. O.** (2001). Moisture effects on the dielectric properties of soils. *IEEE transactions on geoscience and remote sensing*, *39*(1), 125-128.

[40] **Gurbuz, T. U., Aslanyurek, B., Karabulut, E. P., and Akduman, I.** (2014). An efficient nonlinear imaging approach for dielectric objects buried under a rough surface. *IEEE Transactions on Geoscience and Remote Sensing*, *52*(5), 3013-3022.

[41] **Wang, W. Q.** (2013). Two-dimensional imaging of targets by stationary frequency diverse array. *Remote sensing letters*, *4*(11), 1067-1076.

[42] **Geffrin, J. M., Eyraud, C., Litman, A., and Sabouroux, P.** (2009). Optimization of a bistatic microwave scattering measurement setup: From high to low scattering targets. *Radio Science*, *44*(2).

[43] **Akıncı, M. N., Abbak, M., Özgür, S., Çayören, M., and Akduman, I.** (2014). Experimental comparison of qualitative inverse scattering methods. In IEEE Conference on Antenna Measurements & Applications (CAMA), France, Nov. 16-19.

[44] **Colton, D., Haddar, H., and Piana, M.** (2003). The linear sampling method in inverse electromagnetic scattering theory. *Inverse problems*, *19*(6), S105.

[45] **Catapano, I., Crocco, L., and Isernia, T.** (2007). On simple methods for shape reconstruction of unknown scatterers. *IEEE transactions on antennas and propagation*, *55*(5), 1431-1436.

[46] **Haynes, M., and Moghaddam, M.** (2012). Vector green's function for S-parameter measurements of the electromagnetic volume integral equation. *IEEE Transactions on Antennas and Propagation*, *60*(3), 1400-1413.

[47] **Haynes, M., Clarkson, S., and Moghaddam, M.** (2012). Electromagnetic inverse scattering algorithm and experiment using absolute source characterization. *IEEE Transactions on Antennas and Propagation*, *60*(4), 1854-1867.

[48] **Cakoni, F., Cayoren, M., and Colton, D.** (2008). Transmission eigenvalues and the nondestructive testing of dielectrics. *Inverse Problems*, *24*(065016), 15.

[49**] Catapano, I., and Crocco, L.** (2010). A qualitative inverse scattering method for through-the-wall imaging. *IEEE Geoscience and remote sensing letters*, *7*(4), 685-689.

[50] **Akıncı, M. N., and Çayören, M.** (2014). Microwave subsurface imaging of buried objects under a rough air–soil interface. *Remote Sensing Letters*, *5*(8), 703-712.

[51] **Aramini, R., Brignone, M., and Piana, M.** (2006). The linear sampling method without sampling. *Inverse Problems*, *22*(6), 2237.

[52] **Brignone, M., Bozza, G., Aramini, R., Pastorino, M., and Piana, M.** (2008). A fully no-sampling formulation of the linear sampling method for three-dimensional inverse electromagnetic scattering problems. *Inverse Problems*, *25*(1), 015014.

[53] **Kirsch, A.** (1999). Factorization of the far-field operator for the inhomogeneous medium case and an application in inverse scattering theory. *Inverse Problems*, *15*(2), 413.

[54] **Aramini, R., Caviglia, G., Massa, A., and Piana, M.** (2010). The linear sampling method and energy conservation. *Inverse Problems*, *26*(5), 055004.

[55] **Guzina, B. B., Cakoni, F., and Bellis, C.** (2010). On the multi-frequency obstacle reconstruction via the linear sampling method. *Inverse Problems*, *26*(12), 125005.

[56] **Chen, Q., Haddar, H., Lechleiter, A., and Monk, P.** (2010). A sampling method for inverse scattering in the time domain. *Inverse Problems*, *26*(8), 085001.

[57] **Haddar, H., Lechleiter, A., and Marmorat, S.** (2014). An improved time domain linear sampling method for Robin and Neumann obstacles. *Applicable Analysis*, *93*(2), 369-390.

[58] **Griesmaier, R.** (2011). Multi-frequency orthogonality sampling for inverse obstacle scattering problems. *Inverse Problems*, *27*(8), 085005.

[59] **Haynes, M., and Moghaddam, M.** (2011). Multipole and S-parameter antenna and propagation model. *IEEE Transactions on Antennas and Propagation*, *59*(1), 225-235.

[60] **Meaney, P. M., Fanning, M. W., Li, D., Poplack, S. P., and Paulsen, K. D.** (2000). A clinical prototype for active microwave imaging of the breast. *IEEE Transactions on Microwave Theory and Techniques*, *48*(11), 1841-1853.

[61] **Abbak, M., Çayören, M., and Akduman, I.** (2014). Microwave breast phantom measurements with a cavity-backed Vivaldi antenna. *IET Microwaves, Antennas & Propagation*, *8*(13), 1127.

[62**] Bucci, O. M., and Isernia, T.** (1997). Electromagnetic inverse scattering: Retrievable information and measurement strategies. *Radio Science*, *32*(6), 2123-2137.

[63] **Balanis C. A.** Wiley (1989) Advanced engineering electromagnetics.

[64] **Ostadrahimi, M., Mojabi, P., Gilmore, C., Zakaria, A., Noghanian, S., Pistorius, S., and LoVetri, J.** (2011). Analysis of incident field modeling and incident/scattered field calibration techniques in microwave tomography. *IEEE Antennas and Wireless Propagation Letters*, *10*, 900-903.

[65] **Bucci, O. M., Cardace, N., Crocco, L., and Isernia, T.** (2001). Degree of nonlinearity and a new solution procedure in scalar two-dimensional inverse scattering problems. *JOSA A*, *18*(8), 1832-1843.

[66] **Fear, E. C., Meaney, P. M., and Stuchly, M. A.** (2003). Microwaves for breast cancer detection?. *IEEE potentials*, *22*(1), 12-18.

[67] **Bond, E. J., Li, X., Hagness, S. C., and Van Veen, B. D.** (2003). Microwave imaging via space-time beamforming for early detection of breast cancer. *IEEE Transactions on Antennas and Propagation*, *51*(8), 1690-1705.

[68] **Güren, O., Çayören, M., Ergene, L. T., and Akduman, I.** (2014). Surface impedance based microwave imaging method for breast cancer screening: contrast-enhanced scenario. *Physics in medicine and biology*, *59*(19), 5725.

[69] **Catapano, I., Crocco, L., D'Urso, M., and Isernia, T.** (2006). A novel effective model for solving 3-D nonlinear inverse scattering problems in lossy scenarios. *IEEE Geoscience and Remote Sensing Letters*, *3*(3), 302-306.

[70] **Crocco, L., Catapano, I., Di Donato, L., and Isernia, T.** (2012). The linear sampling method as a way to quantitative inverse scattering. *IEEE Transactions on Antennas and Propagation*, *60*(4), 1844-1853.

[71] **Scapaticci, R., Di Donato, L., Catapano, I., and Crocco, L.** (2012). A feasibility study on microwave imaging for brain stroke monitoring. *Progress In Electromagnetics Research B*, *40*, 305-324.

[72] **Montoya, T. P., and Smith, G. S.** (1999). Land mine detection using a ground-penetrating radar based on resistively loaded vee dipoles. *IEEE Transactions on antennas and propagation*, *47*(12), 1795-1806.

[73] **Sato, M., Hamada, Y., Feng, X., Kong, F. N., Zeng, Z., and Fang, G.** (2004). GPR using an array antenna for landmine detection. *Near Surface Geophysics*, *2*(1), 7-13.

[74] **Vertiy, A. A., Gavrilov, S. P., Stepanyuk, V. N., and Voynovskyy, I. V.** (2004, June). Through-wall and wall microwave tomography imaging. In *Antennas and Propagation Society International Symposium, 2004. IEEE* (Vol. 3, pp. 3087-3090). IEEE.

[75] **Akıncı, M. N., Çağlayan, T., Özgür, S., Alkaşı, U., Ahmadzay, H., Abbak, M., Cayoren M., and Akduman, İ.** (2015). Qualitative microwave imaging with scattering parameters measurements. *IEEE Transactions on Microwave Theory and Techniques*, *63*(9), 2730-2740.

[76] **Lechleiter, A.** (2006). A regularization technique for the factorization method. *Inverse Problems*, *22*(5), 1605.

[77] **Bazán, F. S., Francisco, J. B., Leem, K. H., and Pelekanos, G.** (2012). A maximum product criterion as a Tikhonov parameter choice rule for Kirsch's factorization method. *Journal of Computational and Applied Mathematics*, *236*(17), 4264-4275.

[78] **Gazit, E.** (1988). Improved design of the Vivaldi antenna. In IEE Proceedings H-Microwaves, Antennas and Propagation, Apr.

[79] **Chiappe, M., and Gragnani, G. L.** (2006). Vivaldi antennas for microwave imaging: Theoretical analysis and design considerations. *IEEE Transactions on Instrumentation and Measurement*, *55*(6), 1885-1891.

[80] **Zhou, B., Li, H., Zou, X., and Cui, T. J.** (2011). Broadband and high-gain planar Vivaldi antennas based on inhomogeneous anisotropic zero-index metamaterials. *Progress In Electromagnetics Research*, *120*, 235-247.

[81] **Wagner, N., Emmerich, K., Bonitz, F., and Kupfer, K.** (2011). Experimental investigations on the frequency-and temperature-dependent dielectric material properties of soil. *IEEE Transactions on Geoscience and Remote Sensing*, *49*(7), 2518-2530.

[82] **Bobrov, P. P., Repin, A. V., and Rodionova, O. V.** (2015). Wideband frequency domain method of soil dielectric property measurements. *IEEE Transactions on Geoscience and Remote Sensing*, *53*(5), 2366-2372.

[83] **Ellison, W. J., Lamkaouchi, K., and Moreau, J. M.** (1996). Water: a dielectric reference. *Journal of Molecular Liquids*, *68*(2), 171-279.

[84] **Aslanyürek, B., Şahintürk, H., and Çayören, M.** (2014). Microwave imaging of a slightly varying 2-D conducting object through generalized impedance boundary conditions. *IEEE Geoscience and Remote Sensing Letters*, *11*(11), 1851-1855.

[85] **Colton, D., Monk, P., & Cakoni, F.** (2014). *Applications of electromagnetic waves to problems in nondestructive testing and target identification*. DELAWARE UNIV NEWARK.

[86] **Pastorino, M., Randazzo, A., Fedeli, A., Salvadè, A., Poretti, S., Maffongelli, M., Monleone R., and Lanini, M.** (2015). A microwave tomographic system for wood characterization in the forest products industry. *Wood Material Science & Engineering*, *10*(1), 75-85.

CURRICULUM VITAE

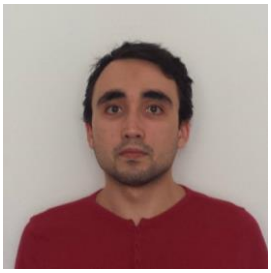

Name Surname **:** Mehmet Nuri AKINCI

Place and Date of Birth **:** Ankara, May 14 1992

E-Mail **:** akincime@itu.edu.tr

EDUCATION **:**

- **B.Sc.** **:** 2013, Istanbul Technical University, Electrical and Electronics Engineering Faculty, Electronics and Communication Department (3.99/4.00)

PROFESSIONAL EXPERIENCE AND REWARDS:

- 142th place in High School Entry Exam (O.K.S.) 2006 out of 1.5 million candidates
- Bronze Medal in TUBİTAK National Physics Olympiads in 2010
- 2nd place in University Entry Exam (O.S.Y.S.) 2010 out of 1.5 million candidates
- Graduated with Highest GPA (3.99/4.00) in Istanbul Technical University in 3 years

PUBLICATIONS, PRESENTATIONS AND PATENTS ON THE THESIS:

- **Akıncı, M. N.**, Çayören, M., 2014. Microwave subsurface imaging of buried objects under a rough air–soil interface, *Remote Sensing Letters*, 5(8), 703-712.
- **Akıncı, M. N.**, Çağlayan, T., Özgür, S., Alkaşı, U., Ahmadzay, H., Abbak, M., Çayören M., Akduman, İ., 2015. Qualitative microwave imaging with scattering parameters measurements, *IEEE Transactions on Microwave Theory and Techniques*, 63(9), 2730-2740.
- **Akıncı, M. N.**, Çağlayan, T., Özgür, S., Alkaşı, U., Abbak, M., Çayören, M., 2015. Experimental Assessment of Linear Sampling and Factorization Methods for

Microwave Imaging of Concealed Targets. *International Journal of Antennas and Propagation*, 1-11.

- **Akıncı, M. N.**, Abbak, M., Özgür, S., Çayören, M., and Akduman, I., 2014: Experimental comparison of qualitative inverse scattering methods. In IEEE Conference on Antenna Measurements & Applications (CAMA), November 16-19, 2014 Nice, France.

OTHER PUBLICATIONS, PRESENTATIONS AND PATENTS:

- **Akıncı, M. N.**, Çayören, M., Akduman, I., 2016. Near-Field Orthogonality Sampling Method for Microwave Imaging, *IEEE Transactions on Microwave Theory and Techniques*, 64(8), 2489 – 2501.

- Abbak, M., **Akıncı, M. N.**, Ertay, A. O., Ozgur, S., Işık, C., Akduman, I., 2016. Wideband Compact Dipole Antenna for Microwave Imaging Applications. *IET Microwaves, Antennas & Propagation*, 1-12.